Modeling optical properties of non-cubical sea salt particles

Franz Kanngießer[1], **Michael Kahnert**[1,2]

[1]Department of Space, Earth and Environment, Chalmers University of Technology, SE-416 96 Gothenburg, Sweden
[2]Research Department, Swedish Meteorological and Hydrological Institute, Folkborgsvägen 17, SE-601 76 Norrköping, Sweden

Key Points:

- The optical properties of dried sea salt aerosol were studied using three different types of model geometries, convex polyhedra, Gaussian random cubes, and superellipsoids.
- Both Gaussian random cubes and superellipsoids were found to provide sufficient flexibility to bring model results in agreement with laboratory measurements of the linear backscatter depolarisation ratio.
- Model geometries strongly deviating from a cubical shape pose the risk of overestimating the linear depolarization ratio and the extinction-to-backscatter ratio.

Corresponding author: F. Kanngießer, `franz.kanngiesser@chalmers.se`

Abstract

Dried sea salt aerosol is commonly represented in aerosol-optics models by ideal cubical particles, while samples reveal that marine aerosol particles frequently display distorted cubical shapes, and they can have more or less rounded edges. In this study three types of non-ideal cuboidal model geometries are investigated, namely, convex polyhedra, Gaussian random cubes, and superellipsoids. Optical calculations were performed at a wavelength of 532 nm using the discrete dipole approximation and the T-matrix method. The main focus is on optical properties relevant to lidar remote sensing, namely, the linear depolarization ratio in the backscattering direction, and the extinction-to-backscatter or lidar ratio. Gaussian random distortions tend to increase the depolarization ratio in relation to that of perfect cubes, while superellipsoids mimicking cubes with rounded edges generally decrease the depolarization ratio. Convex polyhedra can describe randomly distorted cubes. Their computed depolarisation ratios display random fluctuations about those computed for ideal cubes. The results suggest that Gaussian random cubes and superellipsoids are most consistent with the observations if the geometries deviate only mildly from that of an ideal cube. Gaussian random cubes that strongly diverge from cubical shape pose a risk of overestimating both depolarization and extinction-to-backscatter ratio. Superellipsoids that approach octahedral shape yield unrealistically high depolarization ratios. Investigation of size-averaged optical properties of superellipsoids demonstrate that the presence of absorbing material in marine aerosols can have a dramatic effect on the lidar ratio, and its effect on the depolarization ratio can be of comparable magnitude as that caused by rounding of edges.

1 Introduction

Marine aerosol is one of the most abundant aerosol types in the atmosphere (Boucher, 2015). It consists mainly of more or less hydrated sea salt particles as well as biological material (Boucher, 2015; Patterson et al., 2016; Zieger et al., 2017). The aerosol is emitted into the atmosphere by bursting air bubbles in the oceans and by wind tearing off wave crests (Boucher, 2015). Sea water (e.g. Wells, 2011) contains a mixture of different salts in solution, with sodium chloride being the largest salt component. As a consequence sea salt aerosol particles consist of a mixture of different salts, which is dominated by sodium chloride (NaCl) (Pósfai et al., 1995; Tang et al., 1997; Irshad et al., 2009; King et al., 2012; Ueda et al., 2014; Chi et al., 2015).

Marine aerosol provides large surface areas for heterogeneous chemical reactions. It further influences the climate both directly and indirectly, namely, by directly scattering radiation (Murphy et al., 1998; Buseck & Pósfai, 1999; King et al., 2012), and by acting as cloud condensation nuclei, hence impacting cloud reflectivity and precipitation (Boucher, 2015). Furthermore, sea salt aerosol plays an important role in corrosion processes of metals and reinforced concrete structures in coastal areas (Meira et al., 2008).

Large-scale transport models typically contain sea-salt modules that describe the generation, hydration or dehydration, transport, and deposition of marine aerosol (e.g. Foltescu et al., 2005). Evaluation of such models requires the use of long-term data sets with global coverage, with can be obtained from remote sensing observations. The analyses of remote sensing observations, in turn, requires a thorough understanding of the connection between aerosol microphysical properties and optical properties.

Especially in the tropics crystalline sea salt aerosol can play an significant role. The tropical troposphere is commonly characterised by the trade wind inversion, which has a lower boundary within the lowest two kilometres. Please note, that the trade wind inversion does not necessarily coincide with with the top of the atmospheric boundary layer, as discussed by Carrillo et al. (2016) and references therein. Within this inversion layer the moisture content rapidly decreases, so that the troposphere above that inversion layer is extremely dry (Krishnamurti et al., 2013). Aerosol lifted into or above the inversion

layer dries out; as a consequence, sea salt aerosol particles may crystallise as proposed in (Haarig et al., 2017). But even measurements performed in extra-tropical latitudes indicate the potential presence of dried sea salt aerosol (Sakai et al., 2000).

Dried sea salt particles come in cubical or cuboidal shapes, or in shapes deviating slightly from such a reference shape, as images of particle samples indicate (Peart & Evans, 2011; Gwaze et al., 2007; Patterson et al., 2016; King et al., 2012; Zeng et al., 2013; McInnes et al., 1994). Measurements of the dynamic shape factor of artificial sea salt, reported by Zieger et al. (2017), indicate aspherical, cube-like shapes. Less common are irregular shapes, which were reported in (Sakai et al., 2010; Peart & Evans, 2011; Zeng et al., 2013). The shape of salt crystals differs for different salts (Pósfai et al., 1995; Wise et al., 2005). In case of mixtures, such as sea salt, already small amounts of non-NaCl components can alter the shape of the sea salt aerosol particles compared to pure NaCl crystals (Zieger et al., 2017). Thus the chemical composition of sea salt aerosol particles influences both the particle shape and the dielectrical properties, both of which impact the optical properties.

The optical properties, and more specifically the linear depolarization ratio of sea salt aerosol particles have previously been measured in laboratory studies and during lidar field observations. Lab measurements of the linear depolarization ratio in the near-backscattering direction of pure NaCl crystals yielded values of $\delta_{l,179^\circ} = 21\%$ at 532 nm wavelength (Sakai et al., 2010), and $\delta_{l,178^\circ} \approx 25\%$ at 488 nm (Järvinen et al., 2016). For crystalline sea salt at 532 nm a value of $\delta_{l,179^\circ} = 8\%$ was reported(Sakai et al., 2010). Further, the depolarization ratio is dependent on the relative humidity (RH) of the ambient air. At 632.8 nm values of δ_l ranging from 5.6–11.1% for $77\% < RH < 92\%$ and $\delta_l \approx 20\%$ for $RH < 12\%$ for NaCl particles in a lab environment have been reported in the near-backscattering direction, i.e. $\vartheta > 177^\circ$ (Cooper et al., 1974).

While there are various lidar field observations of marine or sea salt aerosol, there are only a limited number of reported measurements of the linear depolarization ratio in combination with reported values of the relative humidity. The combination of measuring the linear depolarization ratio of marine aerosol particles and the relative humidity in the same layer can indicate the presence of dried sea salt aerosol particles. In Table 1 values of linear depolarization ratio and extinction-to-backscatter ratio at 532 nm obtained from lidar field measurements of dried marine aerosol are shown. The classification as marine aerosol is taken from each reference and usually based on backward trajectory analyses.

Sea salt aerosol particles grow with increasing relative humidity by water vapour condensing onto the crystal (Shettle & Fenn, 1979). The crystal gets increasingly dissolved by the condensed water. If the deliquescence point, which for sea salt crystals is at a relative humidity of approximately 70–74% (Tang et al., 1997; Zieger et al., 2017), is reached, the salt crystal becomes fully dissolved in a liquid droplet. A liquid droplet containing dissolved sea salt remains liquid until the relative humidity is below 45–50%(Tang et al., 1997; Zieger et al., 2017), at which point the salt recrystallises. Between values of the relative humidity of ~ 50 and $\sim 70\%$ both crystalline, aspherical and dissolved, spherical sea salt aerosol particles may coexist as a consequence of this hysteresis effect. Therefore, aerosol layers with reported values of relative humidity below 50% (Zieger et al., 2017) are considered to be dried and hence crystalline.

The values reported by Sakai et al. (2000) should be taken with a grain of salt, as they can be partially contaminated by continental aerosol particles. For the measurements conducted on the Atlantic Ocean near Cape Town (Bohlmann et al., 2018) two values of RH were reported. The value of $RH \approx 50\%$ was obtained by a radiosonde and the value of $RH < 40\%$ was taken from the Global Data Assimilation System (GDAS1). Values of δ_l up to 11% for marine aerosol as reported by Groß et al. (2013) indicate the presence of dried sea salt particles, however the lack of reported RH measurements makes

Table 1. Depolarization ratios and extinction-to-backscatter ratios of dried sea salt aerosol particles from lidar measurements at 532 nm and the corresponding relative humidity (RH) of the aerosol layer

location	δ_l (%)	S_p (sr)	RH	reference
Husbands, Barbados	14.8 ± 3.5	25 ± 3	40%	(Haarig et al., 2017)
Atlantic Ocean (near Cape Town)	9	13 ± 3	$< 40\%$ (50%)	(Bohlmann et al., 2018)
Atlantic Ocean (west of Western Sahara)	8	–	∼10%	(Yin et al., 2019)
Tokyo, Japan	10	–	$< 50\%$	(Murayama et al., 1999)
Hagoya, Japan	$10 - 20$	–	$25 - 45\%$	(Sakai et al., 2000)

it difficult to assess this. For a relative humidity of $RH > 80\%$ values of the linear depolarization ratio of $6-7\%$ were reported by Sakai et al. (2012). Based on these field observations as well as the laboratory experiments linear depolarization ratios of up to 20–25% and extinction-to-scatter ratios of up to 25 sr particles can be considered plausible for dried (sea) salt aerosol.

Compared to mineral dust and soot aerosol (see e.g. the studies by Nousiainen and Kandler (2015); Kahnert and Kanngießer (2020) and references therein) the approaches to modeling optical properties of sea salt particles are less studied. Sea salt aerosol particles have been modeled by using spheres (Chamaillard et al., 2006) and cubes (Murayama et al., 1999; Chamaillard et al., 2006; Sakai et al., 2010; David et al., 2013; Haarig et al., 2017). In (Adachi & Buseck, 2015) spheres, cubes, and elongated and flattened cuboids are use as model particles to assess effects on light scattering. In order to model depolarization ratios, cubes were used by Murayama et al. (1999); Sakai et al. (2010); David et al. (2013); Haarig et al. (2017). (Bi, Lin, Wang, et al., 2018) demonstrated the applicability of superellipsoids to model the depolarization of sea salt aerosol particles. In that study superellipsoids resembling rounded cubes, spheres, and rounded octahedra as well as distortions of these base solids by changing the aspect ratio were considered. Sea salt aerosol with a water coating was investigated in regard to the depolarization ratio (Bi, Lin, Wang, et al., 2018), and in regard to the impact on radiative forcing (Wang et al., 2019).

The values of the near-backscattering linear depolarization ratio for pure, crystalline NaCl reported from laboratory measurements by Cooper et al. (1974); Sakai et al. (2010); Järvinen et al. (2016) (note, that the measurements by Cooper et al. (1974); Järvinen et al. (2016) were not performed at $\lambda = 532\,\text{nm}$) are larger than the depolarization ratio for crystalline sea salt, as reported from both laboratory measurements (Sakai et al., 2010) and from most lidar field observations listed in Tab. 1. The images of the salt particles, analysed by Sakai et al. (2010), indicate, that sea salt particles have an irregular, non-cubical shape, whereas pure NaCl particles have regular geometries with sharper edges. The laboratory measurements for pure NaCl with a mode radius of $r = 0.12\,\mu\text{m}$ could be reproduced using cubes with an effective radius of $r_{eff} = 0.5\,\mu\text{m}$ (Sakai et al., 2010). By modeling size averaged linear depolarization ratio, it was found, that cubes, following the same size distribution as the measurements, underestimate the measured depolarization ratio (Bi, Lin, Wang, et al., 2018) by about a factor of 2.

Here the impact of sharp edges and shape distortions on the backscatter linear depolarization ratio and the extinction-to-backscatter ratio (or lidar ratio) of sea salt aerosol particles are investigated. To our knowledge the impact of morphological changes of sea salt particles on the extinction-to-backscatter ratio has not yet been studied.

2 Particle geometries

We want to study to what extent deviations from an ideal cubical shape impact the optical properties. To this end, we perform light-scattering computations for ideal cubes, convex polyhedra, Gaussian random cubes, and superellipsoids. In the latter case, we consider both a cubical and an octahedral reference shape.

2.1 Convex polyhedra

Based on irregularly shaped dust model particles used for radiative forcing calculations by Torge et al. (2011), convex polyhedra were created. N_c points were randomly placed in a Cartesian coordinate system, and around these points a convex hull is placed. This results in an irregular shape with a surface composed of plane faces. The convex hull is constructed using the the quickhull algorithm (Barber et al., 1996) as implemented in the SciPy library for Python (Virtanen et al., 2020). As the points are randomly placed in a Cartesian coordinate system the shape of the convex polyhedron converges to a cubical shape for a sufficiently large number of points N_c. Here N_c =10, N_c =100, and N_c =1000 were used. For each value of N_c five different particle realisations were constructed to capture the variability associated with the random placement of the N_c points, when creating the convex polyhedra. Strictly speaking shapes like cubes or octahedra are convex polyhedra, too. For brevity we use the term "convex polyhedra" to refer to the irregular convex polyhedra, which are neither cubical, nor octahedral.

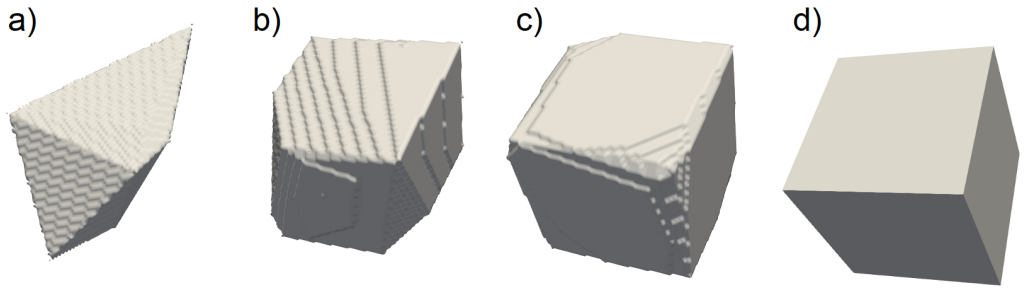

Figure 1. Convex polyhedra with different number of points included in the convex hull N (a–c) and a cube for comparison (d). The number of points increases from left to right: $N_c = 10$ (a), $N_c = 100$ (b) and $N_c = 1000$ (c). The cube corresponds to $N_c \longrightarrow \infty$)

Figure 1 shows examples for such convex polyhedra with a different number of points inside the convex hull. The number of points inside the convex hulls are 10 (Fig. 1a), 100 (Fig. 1b), and 1000 (Fig. 1c). With growing number of points the shape increasingly resembles a cube. For comparison Fig. 1d shows a cube, which corresponds to $N_c \longrightarrow \infty$.

2.2 Gaussian random cubes

By Gaussian random cubes we refer to shapes obtained by superimposing Gaussian random perturbations onto a cube using a modified version of the G-sphere algorithm (Muinonen et al., 1996). The Gaussian random perturbations are described by two different parameters, the relative radial standard deviation σ_{r}, which determines the magnitude of the perturbations, and the correlation angle Γ, which determines the angular scale of the fluctuations. The smaller Γ, the larger the angular frequency of the random

surface perturbations (Muinonen et al., 1996). More specifically, given a surface parameterisation $r_{\mathrm{cube}}(\theta, \phi)$ of the surface of a cube in spherical coordinates, and given the surface parameterisation $r_{\mathrm{GRS}}(\sigma_{\mathrm{r}}, \Gamma; \theta, \phi)$ of a *unit* Gaussian random sphere with radial relative standard deviation σ_{r} and correlation angle Γ (Muinonen et al., 1996), we define the surface parameterisation $r(\theta, \phi)$ of the Gaussian random cube by

$$r(\theta, \phi) = r_{\mathrm{cube}}(\theta) \cdot r_{\mathrm{GRS}}(\sigma_{\mathrm{r}}, \Gamma; \theta, \phi). \tag{1}$$

For the radial standard deviation of the perturbations we chose σ_{r} =0.05, 0.1, 0.15, 0.2, and for the correlation angle $\Gamma = 10°, 20°, 30°,$ and $90°$. For each of the configurations five different stochastic realisations were created to capture the variation due to the random nature of the perturbations. The chosen values were based on the theoretical study on Gaussian random spheres by Muinonen et al. (1996).

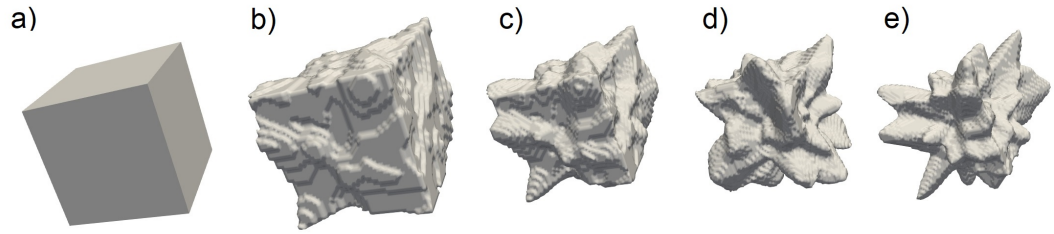

Figure 2. Example of Gaussian random cubes with $\Gamma = 10°$ and increasing radial standard deviation σ_{r}. b) $\sigma_{\mathrm{r}} = 0.05$, c) $\sigma_{\mathrm{r}} = 0.1$, d) $\sigma_{\mathrm{r}} = 0.15$, and e) $\sigma_{\mathrm{r}} = 0.2$ compared to a cube (a)

Figure 2 shows Gaussian random cubes with a fixed correlation angle $\Gamma = 10°$ (b – e) and a cube (a) for comparison. The relative standard deviation of the radius increases by steps of $\Delta\sigma_{\mathrm{r}} = 0.05$ from $\sigma_{\mathrm{r}} = 0.05$ (b) to $\sigma_{\mathrm{r}} = 0.2$ (e).

Comparing with reported images of dried sea salt aerosol (McInnes et al., 1994; Gwaze et al., 2007; Sakai et al., 2010; Peart & Evans, 2011; King et al., 2012; Zeng et al., 2013; Patterson et al., 2016; Sakai et al., 2010) radial standard deviations of $\sigma_{\mathrm{r}} > 0.1$ appear not to be representative of typical atmospheric and laboratory samples. Nevertheless, we include these values here to study the effect of more extreme deviations from cubical shape.

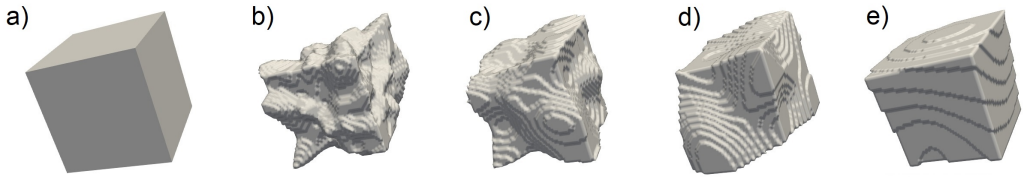

Figure 3. Example of Gaussian random cube with $\sigma_{\mathrm{r}} = 0.1$ and increasing correlation angle Γ. b) $\Gamma = 10°$, c) $\Gamma = 20°$, d) $\Gamma = 30°$, and e) $\Gamma = 90°$ compared to a cube (a)

Figure 3 is analogous to Fig. 2, but showing different values of the correlation angle Γ at a fixed radial standard deviation $\sigma_{\mathrm{r}} = 0.1$ (b–e). The correlation angle is $\Gamma = 10°$ (b), $\Gamma = 20°$ (c), $\Gamma = 30°$ (d), and $\Gamma = 90°$ (e).

2.3 Superellipsoids

Superellipsoids are three dimensional shapes represented by the product super-quadratic curves and can be considered generalisations of ellipsoids (Barr, 1981; Wriedt, 2002). The suitability of superellipsoids for modeling depolarization ratios of mineral dust (Bi, Lin, Liu, & Zhang, 2018) and sea salt aerosol (Bi, Lin, Wang, et al., 2018) were previously demonstrated. Various different solids ranging from cuboids, cylinders, spheres to octahedra can be obtained as realisations of superellipsoids (for examples see (Wriedt, 2002)). The superellipsoidal equation for a Cartesian coordinate system with coordinates x, y, and z is (Barr, 1981; Wriedt, 2002)

$$\left[\left(\frac{x}{a}\right)^{\frac{2}{e}} + \left(\frac{y}{b}\right)^{\frac{2}{e}}\right]^{\frac{e}{n}} + \left(\frac{z}{c}\right)^{\frac{2}{n}} = 1 \tag{2}$$

The particle's extent along the three Cartesian axes x, y and z is determined by a, b, and c, respectively. n and e are the roundness parameters in north-south (or polar) and east-west (or azimutal) direction, respectively, which specify the shape. Variation of n and e allows for flexible modeling of a particle's roundness. Here we follow the approach in (Bi, Lin, Liu, & Zhang, 2018; Bi, Lin, Wang, et al., 2018) by assuming $a = b$ and $n = e$.

To investigate the impact of sharp edges we consider a cube (corresponding to $n = 0$) and slightly rounded cubes ($n = 0.1$ and $n = 0.2$), as well as an octahedron ($n = 2.0$) and rounded octahedra ($n = 1.9$ and $n = 1.8$). A spheroid would have a roundness parameter of $n = e = 1$. The aspect ratio was assumed to be 1, i.e., $a = c$. The superellipsoids used for modeling are shown in Fig. 4. The cube and the rounded cubes are shown in the top row (a–c) and the octahedron and the rounded octahedra are shown the the bottom row (d–f). In both rows the roundness increases from left to right. The sharp-edged shapes are in the left column (a,d), the middle column (b,e) and the right column (c,f) show shapes with slightly rounded shapes.

2.4 Size distribution of marine aerosol

We investigate most optical properties for randomly oriented particles of a definite size. However, atmospheric aerosol particles are typically distributed over a range of sizes. The computation of size-averaged optical properties can become very time consuming. For this reason, we limit our investigation of size-averaged optical properties to cube-like superellipsoids with $e = n =$0, 0.1, and 0.2. For these geometries we can employ the T-matrix method, which is faster than the DDA, but much more limited in the range of possible particle shapes.

We use two different types of size distributions.

1. We consider a monomodal log-normal size distribution

$$n_{\text{mono}}(r_{ve}; N, r_0, \sigma_n) = \frac{N}{r_{ve} \ln \sigma_n \sqrt{2\pi}} \exp\left[-\frac{\ln^2(r_{ve}/r_0)}{2 \ln^2 \sigma_n}\right], \tag{3}$$

   where N is the particle number density, n describes the number of particles per volume element per size interval, r_{ve} is the volume-equivalent radius of the particles, r_0 is the median radius, and σ_n represents the geometric standard deviation. In our calculations we use $\sigma_n = 1.5$ and $r_0 = 0.1, 0.2, \ldots, 1.5\mu$m. Size averaging of the optical properties involves integration of the scattering matrix elements, weighted by the scattering cross section and the size distribution. Numerically, we perform the integration by use of 146 equally spaced particle sizes 0.050, 0.067, ..., 2.509μm.

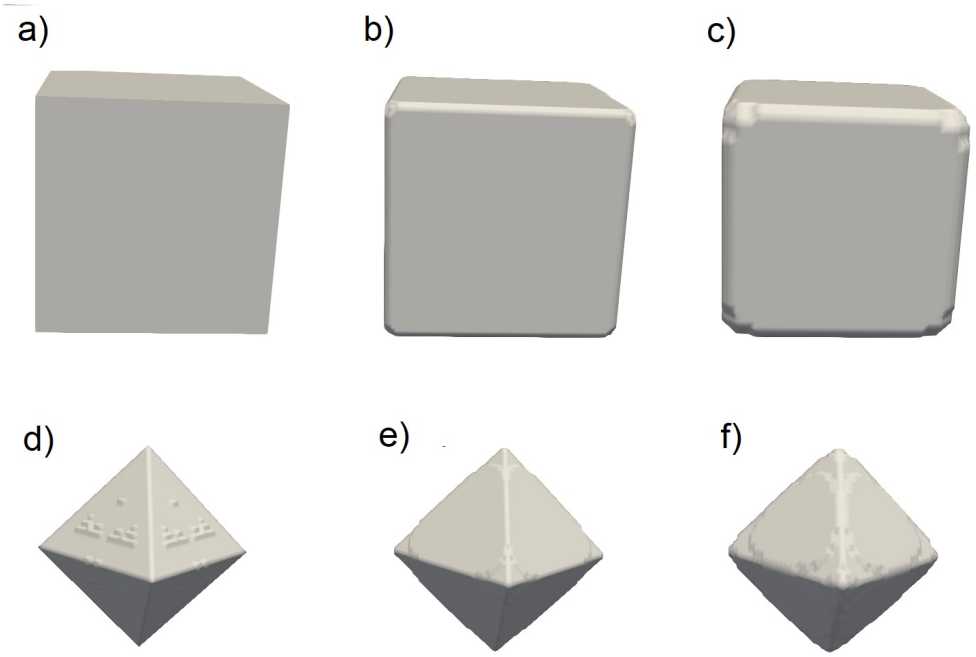

Figure 4. Examples of cube-like superellipsoids (top row) and octahedron-like superellipsoids (bottom row). The roundness increases from left to right. a) and d) show sharp-edged geometries with $n = 0$ and $n = 2$, respectively. b) and c) show geometries with $n = 0.1$, and $n = 1.9$, respectively; and c) and f) show geometries with $n = 0.2$, and $n = 1.8$.

2. Marine aerosol are often best described by a bimodal size distribution. Thus, as a more realistic case, we consider a bimodal log-normal size distribution given by

$$n_{\text{bimodal}}(r_{ve}; N_1, r_{0,1}, \sigma_{n,1}, N_2, r_{0,2}, \sigma_{n,2}) \\ n_{\text{mono}}(r_{ve}; N_1, r_{0,1}, \sigma_{n,1}) + n_{\text{mono}}(r_{ve}; N_2, r_{0,2}, \sigma_{n,2}). \tag{4}$$

For the median radii, geometric standard deviations, and number densities in each mode we use twelve different combinations of parameters given in Table 2 in the study by Porter and Clarke (1997). They are based on observations in the marine boundary layer at winds speed varying between 0.4 to more than 33 m/s. Note, however, that marine aerosol populations at high wind speeds would contain considerable number densities of coarse aerosol. We are limited by computational constraints to particles radii not exceeding 2.509μm. Thus our computation cannot be regarded as covering a similar range of wind speeds as the size distributions given by Porter and Clarke (1997).

For either size distribution, we present the size-averaged optical properties as functions of the effective radius

$$r_{\text{eff}} = \frac{\int_0^\infty n(r_{ve})\, r_{ve}\, \pi r_{ve}^2 \, \mathrm{d}r_{ve}}{\int_0^\infty n(r_{ve})\, \pi r_{ve}^2 \, \mathrm{d}r_{ve}}, \tag{5}$$

where n denotes either the monomodal or the bimodal log-normal size distribution. Thus the effective radius represents the ratio of the third and the second moment of the size distribution. It is a quantity frequently employed for characterising the size of polydisperse particles in light-scattering processes (e.g. (Mishchenko et al., 2002)).

3 Optical modeling

The optical calculations were performed for a wavelength of 532 nm. This is the second harmonic of neodymium-doped yttrium aluminium garnett (Nd:YAG) lasers, which are commonly used in lidar instruments (Wandinger, 2005; Eloranta, 2005).

The refractive index of NaCl as given by Eldridge and Palik (1997) was used in this study, as sea salt is dominated by sodium chloride. Thus we assume $m = 1.5484 + i0$. Note that the imaginary part of the refractive index is zero, i.e., the particles are assumed to be non-absorbing.

(Hänel, 1976) reported slightly different values for dried marine aerosol ($m = 1.55 + i0.059$) and dried sea spray aerosol ($m = 1.55 + i0$). Since Hänel (1976) reported values not directly at $\lambda = 0.532\,\mu$m, the values given here were obtained from linear interpolation. The latter value underscores that the refractive index of NaCl closely agrees with that of sea salt aerosol. In addition to the chemical composition of the dry sea salt the refractive index of sea salt aerosol has a weak dependence on the relative humidity (Shettle & Fenn, 1979; Cotterell et al., 2017).

The calculations were performed at three different volume-equivalent radii $r_{ve} = 0.25\,\mu$m, $0.5\,\mu$m, and $1.0\,\mu$m. This covers a large part of the typical size range for this kind of aerosol, although particles up to radii of $5\,\mu$m are not uncommon. However, the upper end of our size range is constrained by computational capabilities of light-scattering software.

Optical calculations for all particle geometries were performed using the discrete dipole approximation (DDA) code ADDA (Yurkin & Hoekstra, 2007, 2011). The DDA can treat arbitrary geometries, as the scatterer is divided into multiple, fully polarisable volume-elements called dipoles, which are much smaller than the wavelength. The dipoles interact with each other and the incident field, resulting in a set of linear equations, which are solved using standard numerical methods. As a consequence of dividing the scatterer into fully polarisable dipoles arbitrary geometries and inhomogeneous scatterers can be treated.

We also performed T-matrix calculations on superellipsoids. We employed the Tsym code (Kahnert, 2013). This code is highly efficient for particles with discrete symmetries, such as superellipsoids, as it makes use of commutation relations (Schulz et al., 1999) and irreducible representations (Kahnert, 2005) of finite symmetry groups. Here, we extended the Tsym version described by Kahnert (2013) by including the surface parameterisation of superellipsoids into the code. The details are described in the appendix. The Tsym computations serve two main purposes. (i) We employ the T-matrix results for comparison with DDA computations (see below). (ii) DDA computations are prohibitively time consuming for computing optical properties for an entire size distribution. For this reason, we employ the T-matrix method for investigating size-averaged optical properties of superellipsoids (see Sec. 2.4).

The light scattering computations give out the optical cross sections and the full scattering matrix, from which other optical parameters can be calculated. For instance, the extinction-to-backscatter ratio S_p, which, in the context of lidar remote sensing, is frequently referred to as the lidar ratio, can be calculated for a distinct particle size r as (Gasteiger et al., 2011)

$$S_p(r) = 4\pi \frac{C_{\mathrm{ext}}(r)}{C_{\mathrm{sca}}(r) F_{11}(r)}\bigg|_{\vartheta=180^\circ} \tag{6}$$

C_{ext} is the particle's extinction cross section, C_{sca} the particle's scattering cross section, and F_{11} denotes the phase function, which is the (11) element of the normalised Stokes scattering matrix.

The linear backscattering depolarization ratio can be calculated by (Mishchenko & Hovenier, 1995):

$$\delta_l = \left. \frac{F_{11} - F_{22}}{F_{11} + F_{22}} \right|_{\vartheta = 180^\circ}, \tag{7}$$

where F_{22} denotes the (22) element of the normalised Stokes scattering matrix, and ϑ represents the scattering angle. The expression is evaluated in the backscattering direction ($\vartheta = 180^\circ$).

The discrete dipole approximation is derived from the volume-integral equation of electromagnetic scattering under the assumption that the volume elements are much smaller than the wavelength of light. Thus, the dipole spacing is the main parameter that controls the numerical accuracy of the results. To estimate the related numerical uncertainty, the dipole spacing for a superellipsoid with $r_{ve} = 0.5\,\mu$m and $n = e = 0.2$ is varied. In the ADDA code we express the dipole spacing as dipoles per wavelength (dpl). The larger we set the value of dpl, the finer the dipole grid.

Another measure to control the dipole spacing is $|m|kd$, with m being the complex refractive index of the scatterer, $k = 2\pi/\lambda$ the wavenumber in vacuum, and d the dipole spacing. *dpl* and $|m|kd$ can be converted into each other by $|m|kd = 2|m|\pi/dpl$ (Yurkin et al., 2006).

To estimate the impact of the dipole spacing, calculations for a superellipsoid with a roundness parameter $n = e = 0.2$ (i.e., a lightly rounded cube) were performed with different dipole spacing ranging between $dpl = 19$ and $dpl = 160$; the results were compared to T-matrix calculations. The (11), (22), and (12) elements for such a superellipsoid with four different dipole spacings are shown in Fig. 5. The rather coarse dipole spacing of $dpl = 19$ is indicated in dark blue, $dpl = 42$ is depicted by the green line, $dpl = 92$ in purple, and the finest dipole spacing of $dpl = 160$ is represented by the yellow line. The T-matrix results are shown by the light-blue line.

The (11) element of the Stokes scattering matrix shows only comparatively little variation with changing dipole spacing. The different lines for the F_{11} elements are nearly indistinguishable by visual inspection. The (12) and (22) element of the Stokes scattering matrix converge toward the T-matrix results with increasing *dpl*. However, the variation of the DDA results with *dpl* is rather weak. For instance, the 12 and 22 elements for $dpl = 92$ (purple) are hardly distinguishable from $dpl = 160$ (yellow), or from the T-matrix results (light blue).

Figure 6 shows the extinction-to-backscatter ratio S_p (top panel) and the linear depolarization ratio δ_l (bottom panel) of a superellipsoid with $n = e = 0.2$ and $r_{ve} = 0.5\,\mu$m as a function of dipoles per wavelength. The last value, which is separated by the vertical black line from the previous values, shows the T-matrix results. To highlight the changes with increasing dpl, the y-axes in Fig. 6 do not start at zero. Both extinction-to-backscatter ratio and linear depolarization ratio show a weak dependence on the dipole spacing. The extinction-to-backscatter ratio converges with increasing dpl to the T-matrix result. In case of the depolarization ratio the values from the DDA calculations converge more slowly towards the T-matrix result. The values cover a range less than 1 sr in case of S_p and less than 0.015 in case of δ_l. This small variation is in line with the rather small effect of the dipole spacing on the scattering matrix elements.

In order to not overly increase the computational burden we chose a dipole spacing corresponding to $|m|kd \leq 0.4$, or $dpl \geq 25$ respectively. As a consequence differences smaller than $\Delta\delta_l = 0.015$ and $\Delta S_p = 1\,$sr, respectively, cannot be distinguished from artefacts due to dipole spacing. The calculations were performed assuming totally random orientations, by averaging over 1024 different orientations. The orientational averaging is performed internally within ADDA.

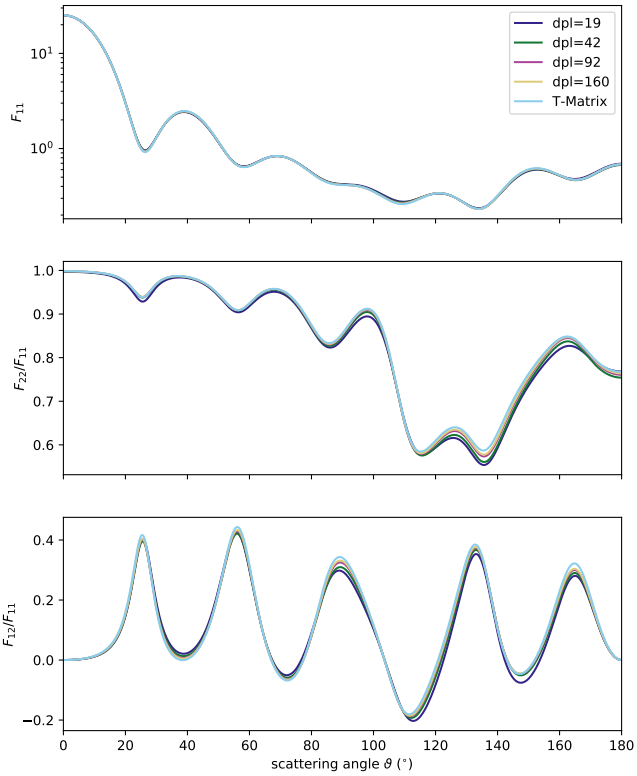

Figure 5. F_{11} (top), F_{22}/F_{11} (middle), and F_{12}/F_{11} (bottom) for different dipole spacing, expressed as dipoles per wavelength *dpl*; $dpl = 19$ in dark blue, $dpl = 42$ in green, $dpl = 92$ in purple, and $dpl = 160$ in yellow. The light-blue line indicates the Matrix elements obtained from T-matrix calculations.

4 Results

4.1 Convex Polyhedra

The ensemble-averaged (11), (22), and (12) elements of the normalised scattering matrix for the different convex polyhedra are shown in Fig. 7. The rows correspond to the matrix elements and the columns to the different volume-equivalent radii. The matrix elements for convex polyhedra based on $N_c = 10$ randomly placed points are shown in dark blue, for shapes with $N_c = 100$ in green, $N_c = 1000$ and for a cube, which corresponds to $N \longrightarrow \infty$ in cyan.

The values of both the convex polyhedra with $N_c = 100$ and $N_c = 1000$ are close to the values from the cubes ($N_c \longrightarrow \infty$), whereas the values for $N_c = 10$ deviate more strongly from the values for the cubes. As the example geometries shown in Fig. 1 indicate, the solids with $N_c = 10$ deviate most from a cubical shape.

Figure 8 shows the size-dependent backscattering cross section C_{bak}, extinction-to-backscatter ratio S_p, and linear backscattering depolarization ratio δ_l for convex poly-

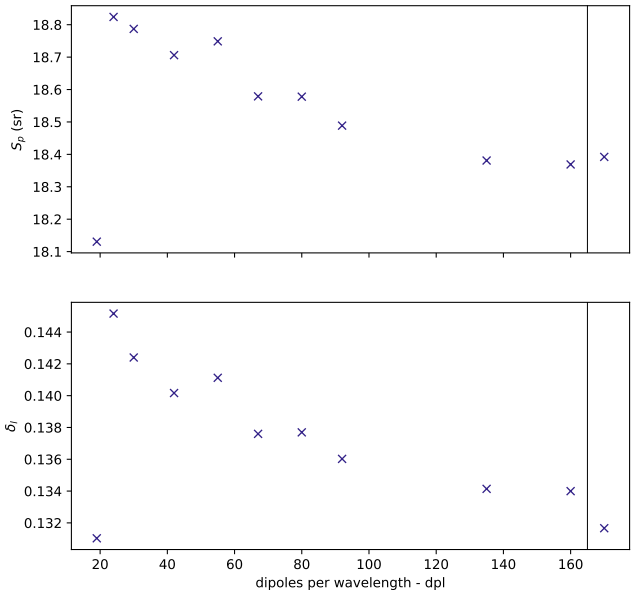

Figure 6. Extinction-to-backscatter ratio (S_p, top panel) and linear depolarization ratio (δ_l, bottom panel) of a superellipsoid with $n = e = 0.2$ and a volume-equivalent radius of $r_{ve} = 0.5\,\mu$m at $\lambda = 0.532\,\mu$m as a function of dipoles per wavelength (*dpl*). Note the different scales of the y-axes.

hedra with $N_=10$ (dark-blue), $N_c = 100$ (green), $N_c = 1000$ (purple), and $N \longrightarrow \infty$ (cyan), which is represented by a cube. With the exception of the cube, the crosses denote the arithmetic mean over five different geometric realisations, and the bars indicate the range between the maximum and minimum of each quantity in the ensemble. To allow for an easier visual inspection the points in Fig. 8, as well as in Figs. 12, and 14 are slightly shifted with respect to the x-axis. With increasing number of points, the variation in the backscattering cross section and in the extinction-to-backscatter ratio is reduced, so that for $N_c = 1000$ the spread in the ensemble is very small. However, this does not hold for δ_l, for which the range for $N_c = 100$ with $r_{ve} > 0.5\,\mu$m is larger than the range for $N_c = 10$. Possibly five different stochastic realisations per N_c do not sufficiently sample from the variety of possible shapes for $N_c = 10$ and hence potentially underestimate the full range of possible values.

The larger deviations in the F_{22}-element in backscattering direction for $N_c = 10$ compared to the cube ($N \longrightarrow \infty$), especially for $r_{ve} = 0.5\,\mu$m and $r_{ve} = 1.0\,\mu$m, are mirrored in the comparatively large differences in the linear depolarization ratio. Compared to the cubical shape the convex polyhedra with $N_c = 10$ give consistently higher δ_l values. For instance, for $r_{\rm ve} = 1\,\mu$m, the depolarization ratio modeled with the convex particles with $N_c = 10$ is around 0.45, which is about twice as high as that obtained with $N_c \geq 100$.

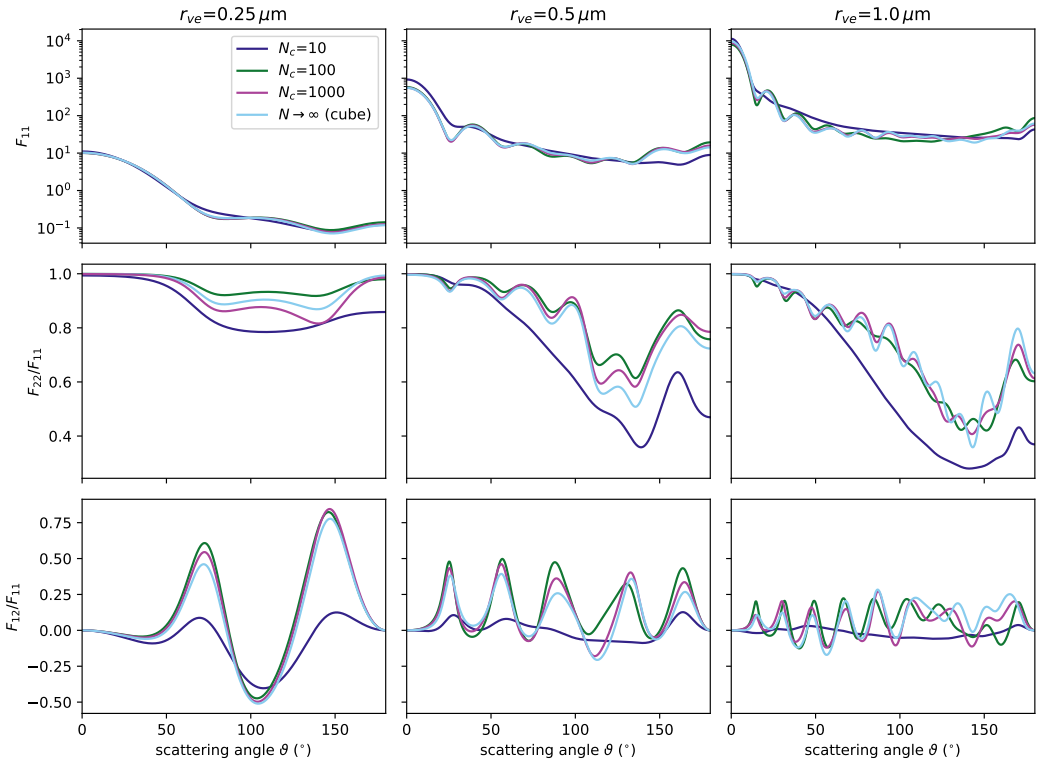

Figure 7. (11), (22), and (12) elements of the normalised scattering matrix for convex polyhedral shapes with $N_c = 10$ (dark blue), $N_c = 100$ (green), $N_c = 1000$ (purple), and for a cube, corresponding to $N \longrightarrow \infty$ (cyan). The (22) and (12) elements are normalised with respect to the (11) element. The matrix elements, with exception for the ones of the cube were averaged over five different geometrical realisations. The columns represent the three different volume-equivalent radii $r_{ve} = 0.25\,\mu$m (left column), $r_{ve} = 0.5\,\mu$m (centre column), and $r_{ve} = 1.0\,\mu$m (right column).

4.2 Gaussian random cubes

As explained in Sec. 2.2 Gaussian random cubes are created by superimposing Gaussian distortions characterised by the correlation angle Γ and the radial standard deviation σ_r on a cube. Figs. 9 – 11 show the (11), (22), and (12) normalised scattering matrix elements for Gaussian random cubes. Each figure shows the matrix elements for a different volume-equivalent radius (Fig. 9 for $r_{ve} = 0.25\,\mu$m, Fig. 10 for $r_{ve} = 0.5\,\mu$m, and Fig. 11 for $r_{ve} = 1.0\,\mu$m). As in Fig. 7 the rows indicate the respective mean matrix elements. The columns in all three figures indicate the radial standard deviation σ_r. The left-most column showed matrix elements for $\sigma_r = 0.05$, the centre-left column for $\sigma_r = 0.10$, the centre-right for $\sigma_r = 0.15$, and the right-most column for $\sigma_r = 0.20$. The colors indicate the correlation angle. The results for a correlation angle of $\Gamma = 10°$ are shown in dark blue, the results for $\Gamma = 20°$ in green, for $\Gamma = 30°$ in light red and for $\Gamma = 90°$ in yellow.

For comparison the corresponding matrix elements of a cube of the same volume-equivalent radius, shown in purple, were added in each panel.

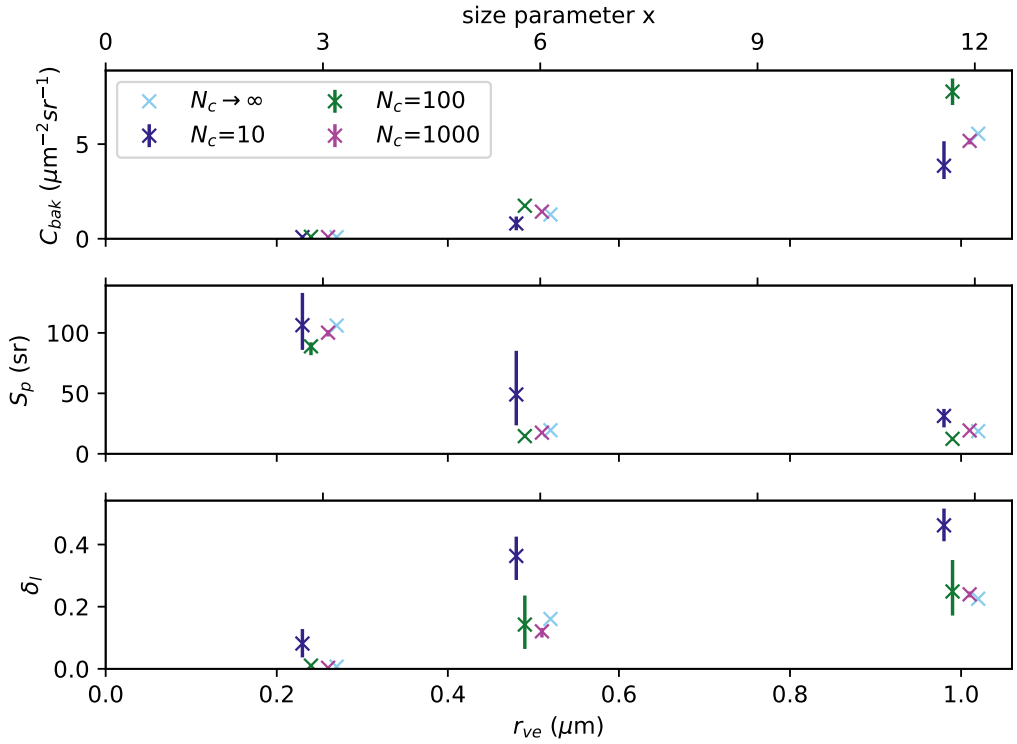

Figure 8. Size-dependent backscattering cross section C_{bak} (top row), extinction-to-backscatter ratio S_p (middle row), linear backscattering depolarization ratio δ_l (bottom row) for cubes, corresponding to $N_c \longrightarrow \infty$ (cyan), $N_c = 10$ (dark blue), $N_c = 100$ (green), and $N_c = 1000$ (purple). Crosses denote the arithmetic mean over five geometric realisations (except for the cube) and the bars indicate the range between the minimum and the maximum value.

Inspection of Figs. 9–11 reveals several interesting features related to the random surface perturbations. Among the more predictable phenomena is a steadily increasing deviation from the scattering matrix elements of the cube with increasing radial standard deviation σ_r (moving from left to right through the columns). Further, by comparing the three figures, we clearly see that the effect of surface perturbations becomes more pronounced for larger particles. For the largest particles (see Fig. 11) it becomes particularly apparent that the impact of the surface perturbation is most pronounced for the shortest correlations angles. For small angles of Γ and high values of σ_r the Gaussian random perturbations of the reference geometry tend to smooth out some of the oscillations in the (12) and (22) elements of the scattering matrix. Finally, we see in all three figures that, overall, the surface perturbation impacts the polarisation and depolarization-related scattering matrix elements S_{12} and S_{22} more dramatically than the phase function S_{11}. While the (11) and (22) elements are fairly sensitive in the backscattering direction, the (12) element is mostly perturbed at angles away from the exact forward and backward-scattering directions.

Figure 12 shows the size-dependent backscattering cross section (left column), extinction-to-backscatter ratio (centre column), and the linear depolarization ratio (right column) for different correlation angles (colors as in Figs. 9–11) and radial standard deviations. The different radial standard deviations are represented in the different rows. The top

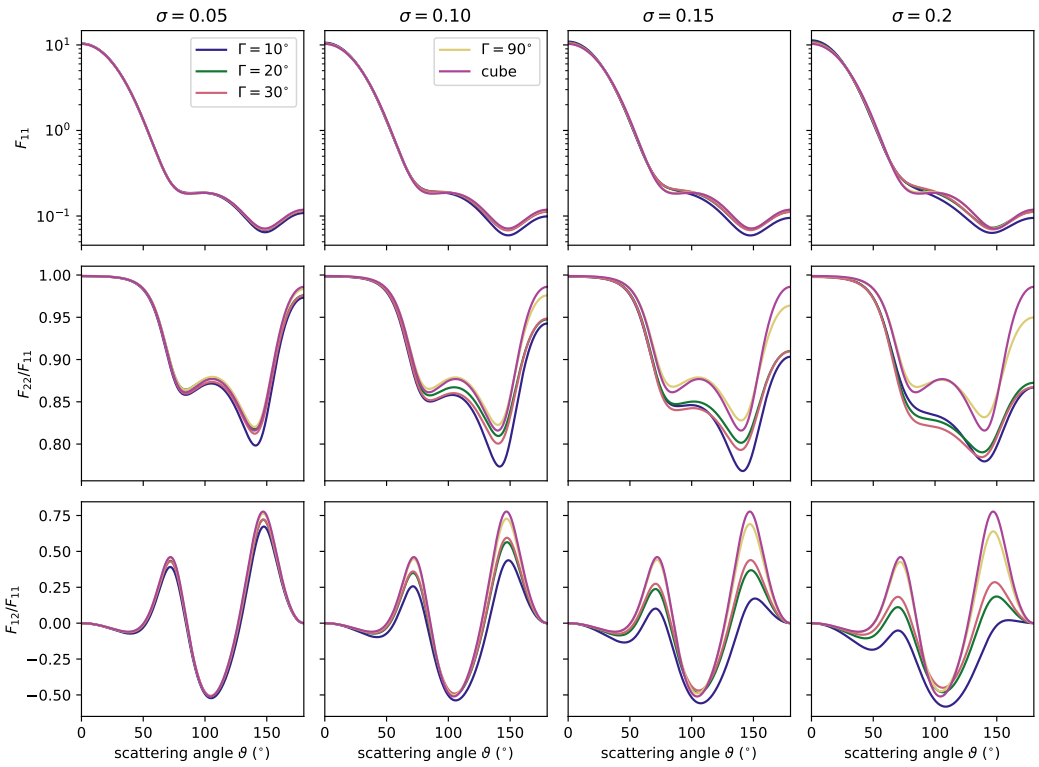

Figure 9. Ensemble-mean of F_{11} (top row), F_{22} (centre row), and F_{12} (bottom row) scattering matrix elements for Gaussian random cubes with a volume equivalent radius of $r_{ve} = 0.25\,\mu$m and different correlation angle Γ (indicated by the colors) and radial standard deviation σ_r (columns). In each plot the corresponding elements of a cube (purple line) were added for comparison. The left columns shows results for $\sigma_r = 0.05$, the centre left for $\sigma_r = 0.1$, the centre right for $\sigma_r = 0.15$, and the right column for $\sigma_r = 0.2$. A correlation angle of $\Gamma = 10°$ is indicated by the dark blue lines, $\Gamma = 20°$ by green, $\Gamma = 30°$ by light red, and $\Gamma = 90°$ by yellow.

row corresponds to $\sigma_r = 0.05$, the second to top row $\sigma_r = 0.1$, the third row $\sigma_r = 0.15$, and the the bottom row to $\sigma_r = 0.2$.

Compared to the cubical shape all Gaussian random cubes introduce a bias in the linear depolarization ratio; they all increase δ_l. The small scale distortions ($\Gamma = 10°, 20°, 30°$) result in depolarization ratios, which deviate stronger from the values obtained for cubes, than the depolarization ratios stemming from the large scale distortion ($\Gamma = 90°$).

4.3 Superellipsoids

Fig. 13 shows the (11) (top row), (22) (middle row), and (12) (bottom row) elements of the scattering matrix F for superellipsoids with different roundness, namely $n = e = 0.0$, (cyan), $n = e = 0.1$ (dark green), $n = e = 0.2$ (light green), $n = e = 1.8$ (light red), $n = e = 1.9$ (purple), and $n = e = 2.0$ (wine). The (22) and (12) elements are normalised with respect to the (11) element. The columns indicate the different sizes, with the results for $r_{ve} = 0.25\,\mu$m shown in the left column, for $r_{ve} = 0.5\,\mu$m in the middle column, and for $r_{ve} = 1.0\,\mu$m in the right column.

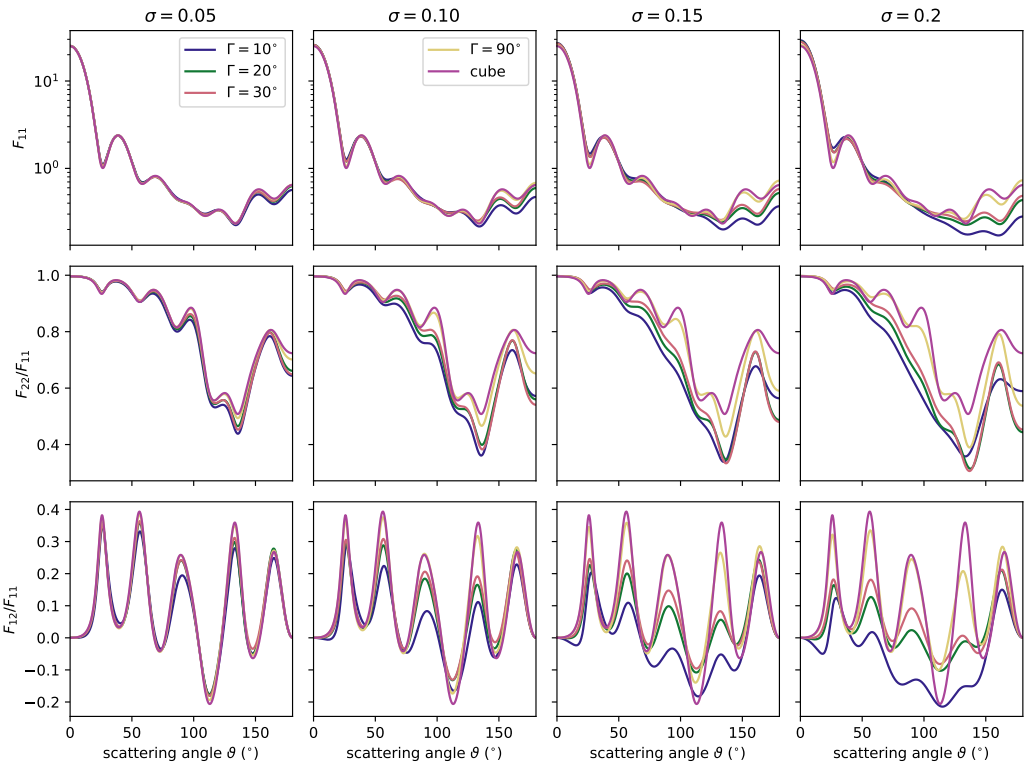

Figure 10. As Fig. 9, but for a volume-equivalent radius of $r_{ve} = 0.5\,\mu$m

Scattering matrix elements for cubes with sharp edges do not strongly differ from those with rounded edges. Similarly, octahedra with sharp and with rounded edges display many similarities. The differences between cube-like and octahedra-like particles are generally larger than the corresponding differences among particles with different degrees of roundness in each of these two groups. However, there is one notable exception. The variability of the (22) element for the octahedron and the rounded octahedra ($n = e = 2.0$, $n = e = 1.8$, $n = e = 1.9$) is larger than that for the cube and rounded cubes ($n = e = 0.0$, $n = e = 0.1$, $n = e = 0.2$).

Analogous to Fig. 8, Fig. 14 shows the size-dependent backscattering cross section C_{bak} (top row), the size-dependent extinction-to-backscatter ratio S_p (middle row), and the linear backscattering depolarization ratio δ_l (bottom row). The different colors refer to the superellipsoids with different roundness parameters n with colors as in Fig. 13.

For $r_{ve} = 1.0\,\mu$m (rounded) octahedra have a higher backscattering cross section than (rounded) cubes, which results in a lower extinction-to-backscatter ratio. Furthermore, the values of the linear depolarization ratio from (rounded) cubes ($\delta_l \approx 0.22$) and (rounded) octahedra ($\delta_l \sim 0.35 - 0.4$) for $r_{ve} = 1.0\,\mu$m deviate stronger from each other, than for the other two sizes. Increasing roundness, i.e. values of the roundness parameter closer to 1, generally decreases the linear depolarization ratio. With exception of the octahedron-like superellipsoids with $r_{ve} = 1.0\,\mu$m, for which the depolarization ratio was increased with increasing roundness.

The results, so far, provide us with valuable information on the importance of overall shape and roundness for modeling optical properties of marine aerosol. However, they are based on comparing model particles with a definite size. We now want to turn our

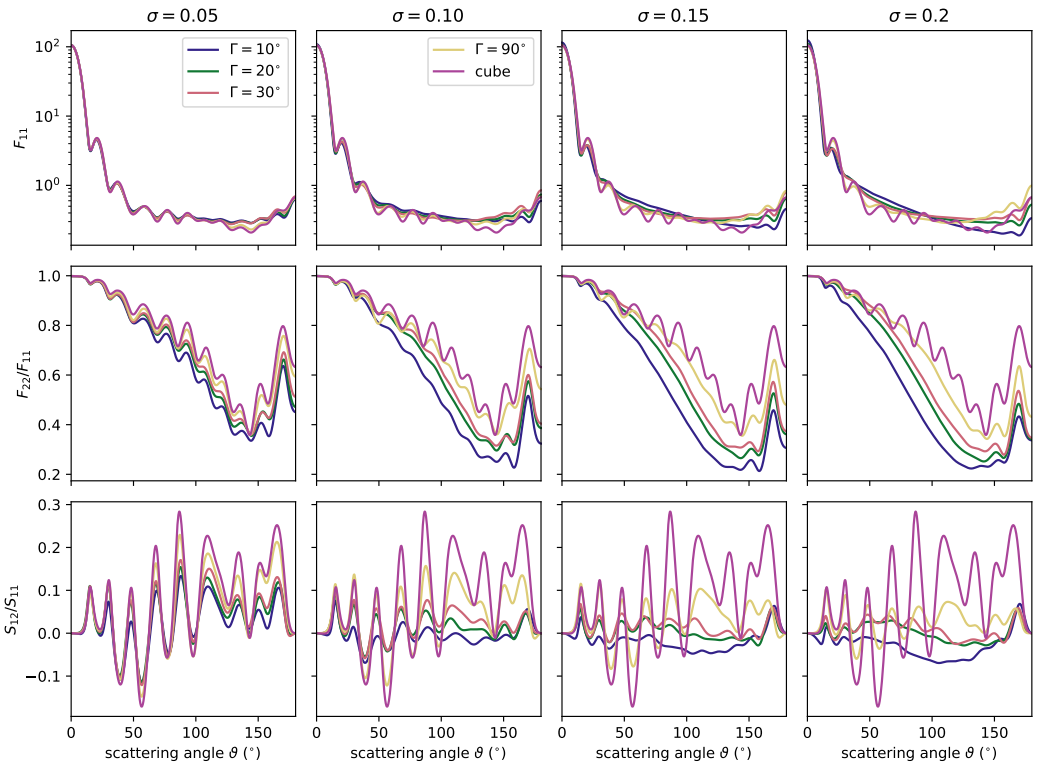

Figure 11. As Fig. 9, but for a volume-equivalent radius of $r_{ve} = 1.0\,\mu$m

attention to size-averaged optical properties of ensembles of randomly oriented cubes with varying degrees of roundness. We also consider two different refractive indices. These results have been computed with the T-matrix program Tsym.

Figure 15 shows the backscattering cross section (top), the lidar ratio (centre), and the linear backscattering depolarization ratio (bottom) as a function of the effective radius. The lines represent different model particles as indicated in the legend and figure caption. Comparison of the left and right column shows that the results hardly depend on whether we assume a monomodal or a bimodel size distribution. (Note the different ranges on the x-axis in either column.)

Most prominently, we see that the impact of roundness on C_{bak} and S_p is dwarfed by that of the imaginary part κ of the refractive index. Increasing the κ from 0 to 0.06 results in a dramatic decrease in C_{bak}, which causes a strong increase in S_p. The strength of this effect grows with increasing $r_{\rm eff}$. By contrast, the corresponding impacts on δ_l are considerably more complex. The impact of roundness is, generally, of comparable magnitude as that of absorption. While roundness generally lowers δ_l for $r_{\rm eff} \leq 1.3, \mu$m relative to cubes with sharp edges, it can have a lowering effect for $r_{\rm eff} > 1.3, \mu$m and $e = n = 0.1$, and an enhancing effect for $e = n = 0.2$. An increase of κ from 0 to 0.06 has little effect for $r_{\rm eff} \leq 0.9, \mu$m, after which δ_l strongly drops with growing $r_{\rm eff}$.

A possible explanation for the latter effect is this. Depolarization by nonspherical particles is strongly influenced by internal resonances induced inside the particle by the incident electromagnetic field. In absorbing particles, these resonances can become quenched. With growing size the absorption cross sections increases, which gradually diminishes the impact of the internal resonance modes. This mainly leaves induced surface currents

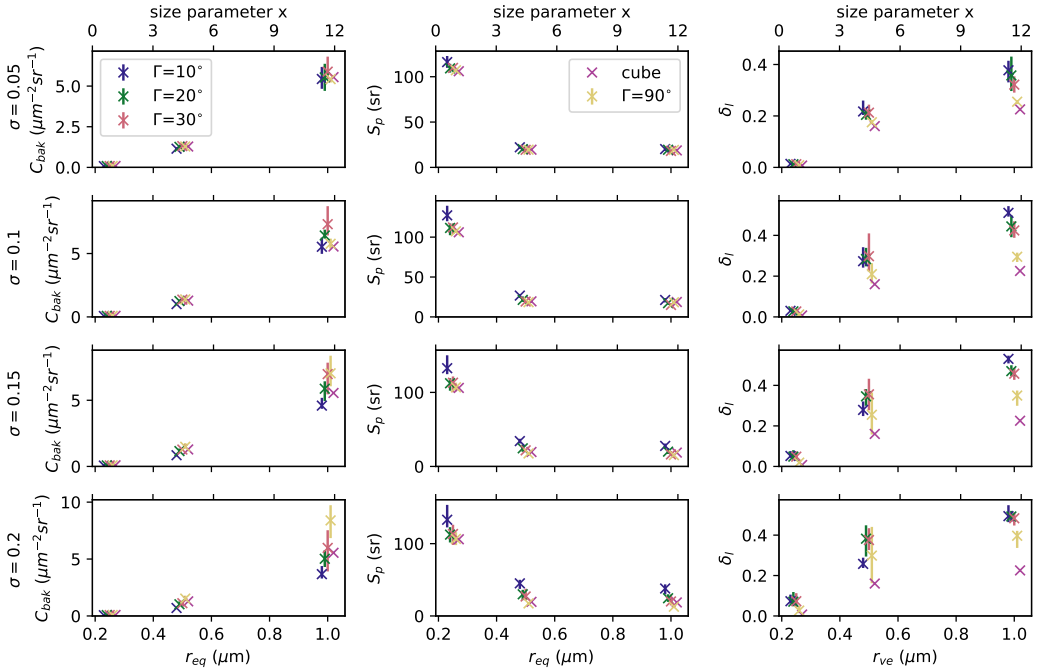

Figure 12. Size-dependent backscattering cross sections C_{bak} (left column), extinction-to-backscatter ratios S_p (middle column), and linear depolarization ratio δ_l (right column) of Gaussian random cubes with different correlation angle Γ and radial standard deviation σ_r. The different values of Γ are indicated by color (with colors as in Fig. 9), and the different values of σ_r are presented in different rows (first row: $\sigma_r = 0.05$, second row: $\sigma_r = 0.1$, third row: $\sigma_r = 0.15$, and bottom row: $\sigma_r = 0.2$). For comparison, each panel shows the corresponding values of cubes in purple.

on the particle surface to impact the depolarization properties of the particle. It is conceivable that the effect of these currents is weaker that that of the resonant modes inside the particle, which would explain the decrease in δ_l with growing particle size.

Figure 16 shows elements of the size-averaged Stokes scattering matrix as a function of scattering angle (x-axis) and effective radius (y-axis). A comparison with Fig. 13 shows that size-averaging smooths out many of the resonance features encountered for monodisperse particles, especially for larger particles. Comparison of rows 1–3 reveals that the rounding of the edges has a rather small effect on both the (11) element (left) and the (12) element (right), and a marginally more pronounced effect on the (22) element (centre column), especially around scattering angles around 100°–150°. By contrast, comparison of rows 1 and 4 shows that an increase in the imaginary part κ of the refractive index has a dramatic effect on the (22) and (12) elements. In the (22) element the deep minimum at scattering angles between 100°–150° becomes considerably more flat with increasing absorption. In the (12) element there is a fairly shallow minimum at scattering angles around 40° for non-absorbing, large particles (top right). As the particles become absorbing, this minimum deepens and shifts toward a scattering angle around 60° (bottom right).

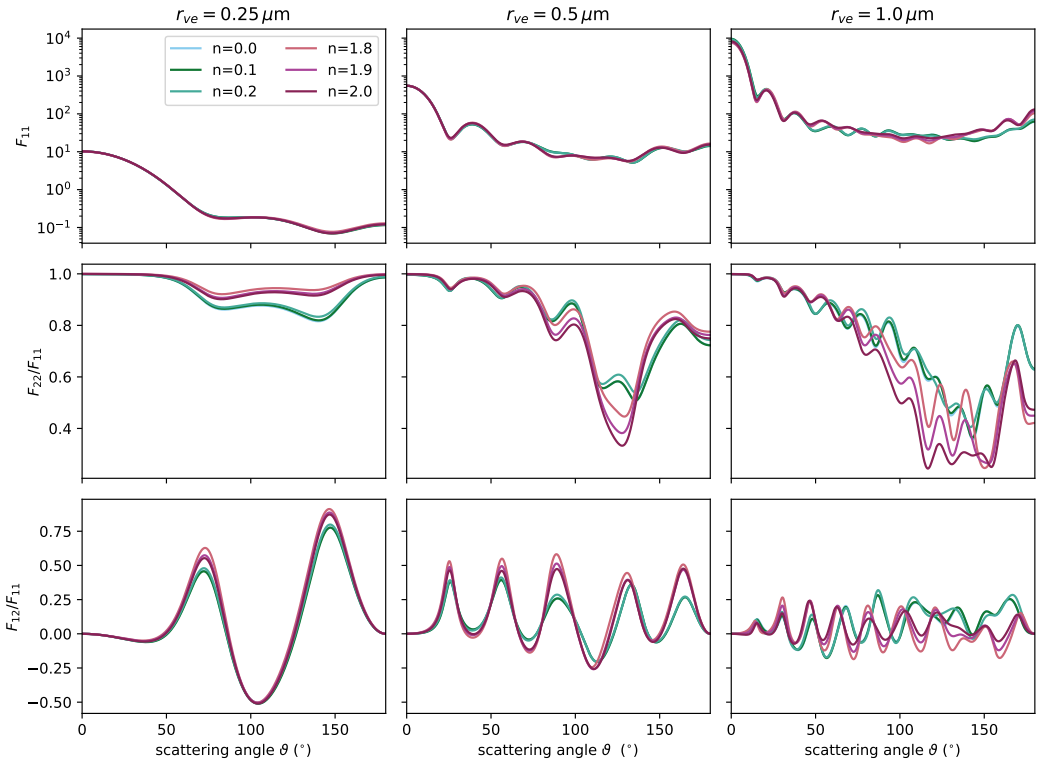

Figure 13. (11) (top row), (22) (centre row), and (12) (bottom row) elements of the normalised scattering matrix F for different superellipsoids with $n = e = 0.0$, corresponding to a cube (cyan), $n = e = 0.1$ (dark green), $n = e = 0.2$ (light green), $n = e = 1.8$ (light red), $n = e = 1.9$ (purple), and $n = e = 2.0$, corresponding to a octahedron (wine). The (22) and (12) elements are normalised with respect to the (11) element. The columns represent the three different volume-equivalent radii $r_{ve} = 0.25\,\mu$m (left column), $r_{ve} = 0.5\,\mu$m (centre column), and $r_{ve} = 1.0\,\mu$m (right column).

5 Discussion

Lidar field observations, as listed in Tab. 1, suggest that the linear backscattering depolarization ratio of marine aerosol lies in the range 0.08–0.20. Comparing the results of scattering calculations for single particle sizes with such field measurements can only serve as a consistency check, not as a conclusive validation. That being said, we do find in Fig. 14 that octahedral particles with or without rounded edges yield linear depolarization ratio that can far exceed the values reported in field measurements. Cubes with and without rounded edges lie closer to the reported range, although at the higher end. Similarly, we saw in Fig. 12 that, at least for large particle radii, δ_l modeled with Gaussian random cubes lies closer to typical field observations when assuming a correlation angle at the higher end, e.g. $\Gamma \sim 90°$, and radial standard deviations not in excess of 0.05. Small correlation angles can strongly enhance δ_l. We also saw in Fig. 8 that convex polyhedra that strongly deviate from cubical shape give unrealistically high δ_l values. Irregular shapes that only mildly deviate from cubical shape are closer to δ_l=0.20. All of these results point into the same direction, namely, that the depolarization of marine aerosols is likely to be best described by particle shapes that display only mild deviations from the shape of an ideal cube.

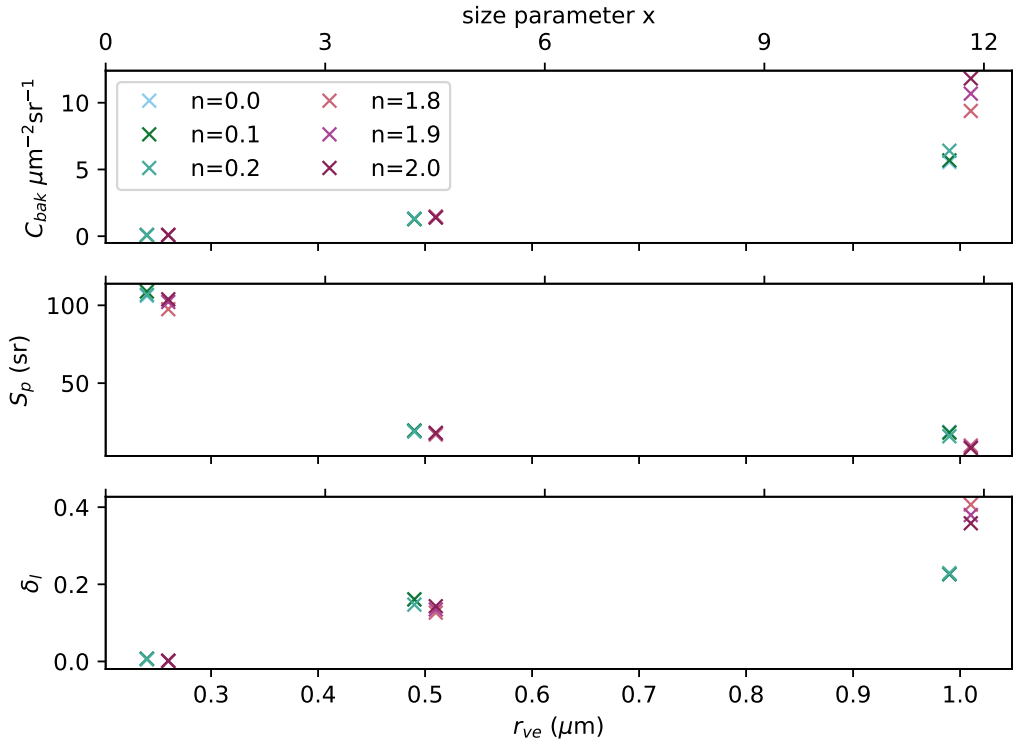

Figure 14. Size-dependent backscattering cross section C_{bak} (top row), extinction-to-backscatter ratio S_p (middle row), linear backscattering depolarization ratio δ_l (bottom row) for superellipsoids with different roundness parameters n. The colors are as in Fig. 13. To better distinguish the values the radius values were shifted around the actual radius.

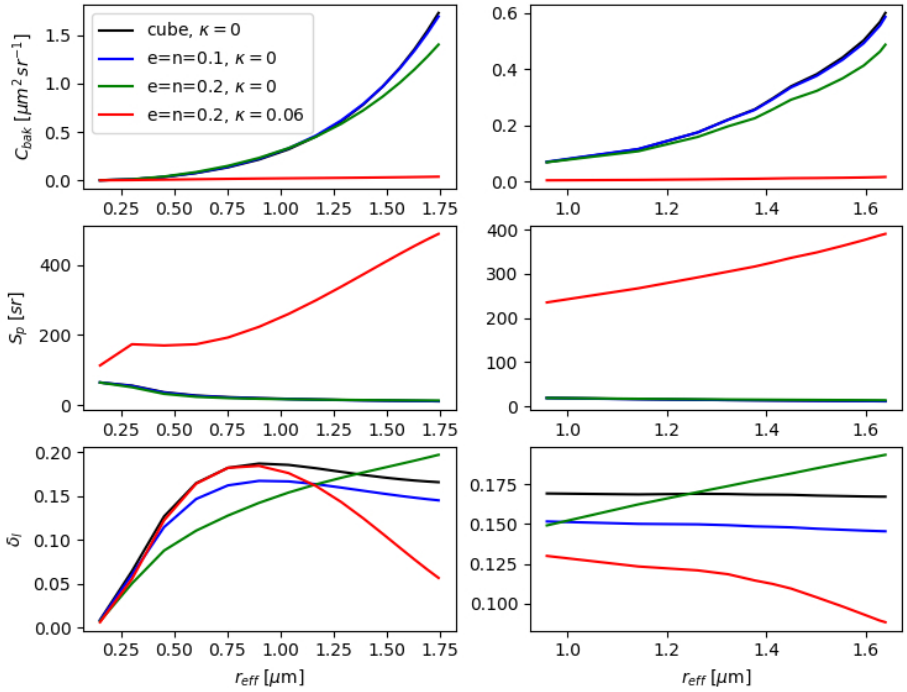

Figure 15. Size-averaged results for C_{bak} (top), S_p (centre), and δ_l (bottom) as a function of the effective radius r_{eff}. The lines show non-absorbing cubes with sharp edges (black), non-absorbing cubic superellipsoids with $e = n = 0.1$ (blue) and $n = e = 0.2$ (green), as well as absorbing superellipsoids ($e = n = 0.2$) with an imaginary part of the refractive index $\kappa = 0.06$ (red). The left row shows results averaged over log-normal monomodal size distributions, the right one over bimodal log-normal size distributions.

How can we explain field observations of δ_l as low as 0.08 as by Yin et al. (2019)? The bottom row in Fig. 15 suggests that there are several possible causes. Aerosol ensembles dominated by small particles with effective radii up to 0.35μm can give rise to such low δ_l values. However, such a situation is unlikely to be encountered in the atmosphere, as we can see by inspecting the right column in Fig. 15. The range of effective radii on the x-axis are derived from the size distributions given by Porter and Clarke (1997), which include wind speeds as low as 0.4 m/s. Even under such conditions the marine aerosols rarely have effective radii less than 1μm.

Another possible effect is observed for effective radii up to 1μm. Rounding of edges can lower depolarization by an amount that depends on the degree of rounding, corroborating results by Bi, Lin, Wang, et al. (2018). Further, for particles with r_{eff} larger than 0.9μm, the presence of absorbing material can significantly quench depolarization. The exact chemical composition (and hence the refractive index) and its size dependence is unknown. However, as most marine aerosols can be assumed to be in the size range where absorption can become important, this is a potentially important topic.

Finally, for high relative humidity (RH) adsorption of water will inevitably suppress depolarization, as the particles will become increasingly spherical. However, high

RH values were deliberately excluded in Table 1; marine aerosol with adsorbed water are outside the scope of our discussion.

Measurements of the extinction-to-backscatter ratio of dried sea salt aerosol are sparse. The two reported values, as can be inferred from Tab. 1, indicate a range between 13–25 sr. Owning to this limited amount of observations it is particularly challenging to draw conclusions. Irrespective of the shape calculated values of the extinction-to-backscatter ratio for $r_{ve} = 0.25\,\mu$m are in the order of $\sim 100\,$sr and thereby exceed the range of the reported values by far. For both $r_{ve} = 0.5\,\mu$m and $r_{ve} = 1.0\,\mu$m the values of S_p are below 25 sr. A notable exception are the convex polyhedra with $N_c = 10$ and Gaussian random cubes with small correlation angle and large radial standard deviation, both types strongly deviate from the cubical base shape. Analogous to the values of the linear depolarization ratio Gaussian random cubes, which deviate less from the cubical shape (i.e. have low radial standard deviations and high correlation angles) result in values of the extinction-to-backscatter ratio, that are closest to the values obtained from cubes. Thus, the results point in a similar direction as the results for the depolarization ratio; the stronger the particle shape deviates from a cubical base shape, the stronger the deviation in extinction-to-backscatter ratio from the field observations. This implies that strongly non-cubical shapes pose a risk of overestimating not only the depolarization ratio, but also the extinction-to-backscatter ratio. However, the results for superellipsoids in form of (rounded) octahedra with $r_{ve} = 1.0\,\mu$m give less clear indications. They result in lower values of the extinction-to-backscatter ratio ($\sim 8\,$sr), than (rounded) cubes ($\sim 20\,$sr). At the same time they pose a risk of overestimating the values of the linear depolarization ratio with $\delta_l = 0.36$ compared to $\delta_l = 0.23$ for cubes. While (rounded) octahedra may help explaining values of the extinction-to-backscatter ratio of $S_p = 13\pm 3\,$sr as reported by Bohlmann et al. (2018), they are unlikely to explain the simultaneously low values of the linear depolarization ratio of $\delta_l = 0.09$ reported by Bohlmann et al. (2018) for the same aerosol layer.

While the values of S_p for individual particles may exceed 25 sr, size averaging reduces the risk of overestimating S_p, as Fig. 15 indicates. Size distributions of non-absorbing (rounded) cubes with effective radii smaller than $0.5\,\mu$m, which are rare under atmospheric conditions, still pose a risk of overestimating the extinction-to-backscatter ratio. However, for larger effective radii the size-averaged model results are in line with the lidar field observations. However, the impact of size-averaging on the optical properties for convex polyhedra, (rounded) octahedra and Gaussian random cubes has not been studied, Fig. 15 suggests, that high values of S_p for individual particles at a single size do not allow for dismissing the entire geometry.

Further, cubical model particles, which follow the same size distribution as particles investigated during a laboratory experiment (reported by Sakai et al. (2010)), were found to underestimate the measurements of the linear depolarization ratio in near-backscattering direction (Bi, Lin, Wang, et al., 2018). (Bi, Lin, Wang, et al., 2018) reconciled measurements and model results by modifying the particles' aspect ratio. After changing the aspect ratio of the superellipsoids the depolarization ratio may increase with increasing roundness parameter (Bi, Lin, Wang, et al., 2018). Superimposing Gaussian random perturbations on a cube increases the linear depolarization ratio. Thus, they provide an additional way of reducing the offset between laboratory measurements and model particles with respect to the depolarization ratio.

6 Conclusion

With exception of the study by Bi, Lin, Wang, et al. (2018), in which superellipsoids were used, the linear depolarization ratio of sea salt particles was previously modeled assuming cubes (Murayama et al., 1999; Sakai et al., 2010; David et al., 2013; Haarig et al., 2017). Here the suitability of three different shape types, convex polyhedra, su-

perellipsoids, and Gaussian random cubes, to model both linear depolarization and extinction-to-backscatter ratio was investigated. In general the comparison of the modeling results with field and laboratory measurements reveals that geometries that depart too strongly from a cubical reference shape pose a high risk of overestimating linear depolarization and extinction-to-backscatter ratio. Compared to cubical reference geometries rounded cubes, obtained from superellipsoids, decrease the depolarization with increasing roundness, while Gaussian random cubes increase the depolarization. An ensemble of randomized, nearly cubical convex polyhedra yield linear depolarization ratio that appear to scatter uniformly about that of ideal cubes.

Thus, it appears that convex polyhedra can be employed for computing unbiased uncertainty estimates for cubical model particles, i.e., they can be employed for assessing the error introduced by neglecting random distortions and rounding of edges. Such uncertainty assessments would be useful for solving inverse problems, e.g., in retrieval algorithms or data assimilation of remote sensing observations of dried marine aerosol particles (e.g. Haarig et al., 2017). Both superellipsoids (see Bi, Lin, Wang, et al., 2018) and Gaussian random cubes can provide ways to reconcile measurements and model particles by tuning the roundness and surface deformation parameters, respectively. Combining roundness and random surface distortions would provide us with another viable model to assess model errors. This is essential in inverse modeling. It is known from studies on the depolarization properties of mineral dust (Kahnert et al., 2020) that unbiased error estimates are best obtained by combining different models of randomised geometries.

Owing to the high computational demands of the discrete dipole approximation, our study on size-averaged optical properties was limited to superellipsoids modeled with the T-matrix method. One of the main findings was that the presence of absorbing material in marine aerosols can dramatically increase the lidar ratio. Its effect on the depolarisation ratio is dependent on the effective aerosol radius; but it is, generally, of comparable magnitude as that related to rounding of edges.

Here only crystalline sea salt aerosol without any water coating was investigated. Adding a liquid water coating would extend the applicability of the model particles discussed here towards higher values of relative humidity. Further laboratory studies combining measurements of the optical and the microphysical properties of dried sea salt aerosol particles can provide additional guidance regarding the choice and/or refinement of particle models.

Acknowledgments

We acknowledge funding by the Swedish Research Council (*Vetenskapsrådet, dnr 2016-03499*) and by the Swedish National Space Agency (*Rymdstyrelsen, dnr 126/19*). The authors declare no conflicts of interest. The calculations were partially performed on resources at Chalmers Centre for Computational Science and Engineering (C3SE) provided by the Swedish National Infrastructure for Computing (SNIC). Maxim Yurkin and Alfons Hoekstra are acknowledged for making their ADDA code publicly available. We are grateful to Karri Muionen for providing the G-sphere code. The data shown in the figures is available under: `http://doi.org/10.5281/zenodo.3977898`

Appendix A Parameterisation of superellipsoids in spherical coordinates

In Waterman's T-matrix method, we need to evaluate vector products of vector spherical wavefunctions $\mathbf{\Psi}^{(j)}_{l,m,q}(r(\theta,\phi),\theta,\phi)$, where l, m, q are the degree, order, and mode, and where j denotes the kind of the vector wavefunctions. The surface integrals are evalu-

ated at the surface $r(\theta, \phi)$ of the particle. Thus, to use Waterman's method we need to have a parameterisation of the particle surface in spherical coordinates.

We start from the implicit equation (2) for the surface of a superellipsoid given in Cartesian coordinates by

$$\left(\left| \frac{x}{a} \right|^{2/e} + \left| \frac{y}{b} \right|^{2/e} \right)^{e/n} + \left| \frac{z}{c} \right|^{2/n} = 1. \tag{A1}$$

The parameters a, b, c, n, and e are positive real numbers. a, b, and c characterise the extend of the particle along the three Cartesian axes, n is a roundness parameter in the polar (north-south) direction, and e is a roundness parameter in the azimuthal (east-west) direction. The superellipsoids are convex for n, $e \in (0, 2)$.

We introduce the following bracket notation:

$$[\xi]^\alpha = \mathrm{sgn}(\xi)|\xi|^\alpha. \tag{A2}$$

Then an explicit parameterisation is given by

$$\begin{aligned} x &= a[\cos u]^n\,[\cos v]^e && \text{(A3)}\\ y &= b[\cos u]^n\,[\sin v]^e && \text{(A4)}\\ z &= c[\sin u]^n && \text{(A5)}\\ & u \in [-\pi/2, \pi/2], \quad v \in [-\pi, \pi]. && \text{(A6)} \end{aligned}$$

It is elementary to verify by direct substitution into (A1) that this parameterisation, indeed, describes the surface of a superellipsoid. However, (u, v) are not spherical coordinates, as required by Waterman's T-matrix method.

To derive a parameterisation in spherical coordinates (θ, ϕ), we need a parameter transformation $(u, v) \mapsto (\theta, \phi)$. To this end, we compute

$$\frac{y}{x} = \tan\phi = \frac{b}{a}\,[\tan(v + k\pi)]^e, \quad k \in \mathbb{Z}, \tag{A7}$$

or

$$\tan(v + k\pi) = \left[\frac{a}{b} \tan\phi \right]^{1/e}, \tag{A8}$$

where we explicitly indicated the periodicity of the tangent. The choice of k becomes important when computing $\phi = \arctan(y/x)$. Making appropriate case distinctions for the four quadrants, we find that $k = 0$ for $\phi \in [0, \pi/2)$, $k = 1$ for $\phi \in [\pi/2, \pi)$, $k = -1$ for $\phi \in [\pi, 3\pi/2)$, and $k = -2$ for $\phi \in [3\pi/2, 2\pi)$. Thus we obtain the following parameter transformation

$$v(\phi) = \arctan\left(\left[\frac{a}{b} \tan\phi \right]^{1/e} \right) + k\pi \tag{A9}$$

$$k = \begin{cases} 0 & : \ \phi \in [0, \pi/2) \\ 1 & : \ \phi \in [\pi/2, \pi) \\ -1 & : \ \phi \in [\pi, 3\pi/2) \\ -2 & : \ \phi \in [3\pi/2, 2\pi) \end{cases} \tag{A10}$$

To obtain an analogous parameter transformation for u, we consider

$$\frac{\sqrt{x^2 + y^2}}{z} = \tan\theta = \frac{1}{c}\,\frac{[\cos u]^n}{[\sin u]^n} \left\{ a^2 |\cos v|^{2e} + b^2 |\sin v|^{2e} \right\}^{1/2}, \tag{A11}$$

or

$$[\tan u]^n = \frac{1}{c} \cot\theta \sqrt{w}, \tag{A12}$$

where

$$w(v(\phi)) = a^2|\cos v|^{2e} + b^2|\sin v|^{2e} \tag{A13}$$

To solve for u, we make a case distinction. For $\theta \in [0, \pi/2)$, $\cot\theta > 0$. Then we must have $\tan u > 0$, which implies $u \in [0, \pi/2)$. Then $u = \arctan\{(1/c)\cot\theta\sqrt{w}\}^{1/n}$. Similarly, for $\theta \in [\pi/2, \pi)$ we find $u = -\arctan\{-(1/c)\cot\theta\sqrt{w}\}^{1/n}$. This can be summarised as follows

$$u(\theta,\phi) = S\arctan\left\{\frac{S}{c}\cot\theta\sqrt{w(v(\phi))}\right\}^{1/n} \tag{A14}$$

$$S = \begin{cases} 1 & : \quad \theta \in [0, \pi/2) \\ -1 & : \quad \theta \in [\pi/2, \pi) \end{cases} . \tag{A15}$$

Equations (A9), and (A14) in conjunction with (A10), (A13), and (A15) provide us with the desired parameter transformation $(u, v) \mapsto (\theta, \phi)$. Substitution into Eqs. (A3)–(A5) in conjunction with $r = \sqrt{x^2 + y^z + z^2}$ gives us the required parameterisation $r(\theta, \phi)$ of the superellipsoid surface in spherical coordinates.

To evaluate the surface integrals in Waterman's method, we also need to express the surface element $\mathrm{d}\sigma$ on the surface of the particle in spherical coordinates, i.e., we need to obtain $\mathrm{d}\sigma = |\partial\mathbf{r}/\partial\theta \times \partial\mathbf{r}/\partial\phi|\,\mathrm{d}\theta\,\mathrm{d}\phi$. In principle, we could now proceed and compute expressions such as $\partial r/\partial\theta = (\partial r/\partial u)\,(\partial u/\partial\theta)$. It turns out that we encounter singularities in terms such as $\partial u/\partial\theta$. Therefore, we do well to first bring the parameter transformations into a more tractable form.

Inspection of Eqs. (A3)–(A5) shows that we never need the parameters u and v directly, but only $\cos u$, $\sin u$, $\cos v$ and $\sin v$. We can make use of the identities

$$\sin(\arctan x) = \frac{x}{\sqrt{1+x^2}} \tag{A16}$$

$$\cos(\arctan x) = \frac{1}{\sqrt{1+x^2}}, \tag{A17}$$

and we abbreviate

$$p = \left\{S\frac{\sqrt{w}}{c}\cot\theta\right\}^{1/n} = \left[\frac{\sqrt{w}}{c}\cot\theta\right]^{1/n} \tag{A18}$$

$$q = \left[\frac{a}{b}\tan\phi\right]^{1/e} . \tag{A19}$$

This yields

$$\sin u = S\frac{p}{\sqrt{1+p^2}} \tag{A20}$$

$$\cos u = \frac{1}{\sqrt{1+p^2}} \tag{A21}$$

$$\sin v = (-1)^m\frac{q}{\sqrt{1+q^2}} \tag{A22}$$

$$\cos v = (-1)^m\frac{1}{\sqrt{1+q^2}}, \tag{A23}$$

whence

$$w = \frac{a^2 + b^2(q^2)^e}{(1+q^2)^e}. \tag{A24}$$

and

$$\begin{aligned} r^2 &= x^2 + y^2 + z^2 \\ &= |\cos u|^{2n}(a^2|\cos v|^{2e} + b^2|\sin v|^{2e}) + c^2|\sin u|^{2n} \\ &= \frac{w + c^2(p^2)^n}{(1+p^2)^n}, \end{aligned} \tag{A25}$$

where we have used the definition of w in Eq. (A13) as well as Eqs. (A20) and (A21). Backsubstitution of the definitions of p and q, Eqs. (A18) and (A19), into these expressions yields

$$r(\theta,\phi) = \left\{ \frac{w}{\left\{ (\sin^2\theta)^{1/n} + \left(\frac{w}{c^2}\cos^2\theta\right)^{1/n} \right\}^n} \right\}^{1/2} \tag{A26}$$

$$w(\phi) = \frac{a^2(1+\tan^2\phi)}{\left\{ 1 + \left(\frac{a^2}{b^2}\tan^2\phi\right)^{1/e} \right\}^e}. \tag{A27}$$

The expression for r is manifestly regular for all θ. (Recall that $n > 0$.) Also, as we approach a singularity of $\tan\phi$, w approaches b^2. Thus, w and r are regular for all values of ϕ.

It is now straightforward, although a bit lengthy, to compute $\partial r/\partial\theta$ and $\partial r/\partial\phi$=$(\partial r/\partial w)\,(\partial w/\partial\phi)$. With the abbreviation

$$t = \tan^2\phi, \tag{A28}$$

the final result is

$$\frac{\partial r}{\partial\theta} = -\frac{w}{r}\,\frac{\cos\theta\,[\sin\theta]^{\frac{2}{n}-1} - \left(\frac{w}{c^2}\right)^{1/n}\sin\theta\,[\cos\theta]^{\frac{2}{n}-1}}{\left\{ (\sin^2\theta)^{1/n} + \left(\frac{w}{c^2}\cos^2\theta\right)^{1/n} \right\}^{n+1}} \tag{A29}$$

$$\frac{\partial r}{\partial\phi} = \frac{a^2}{r}\,\frac{(\sin^2\theta)^{1/n}}{\left\{ (\sin^2\theta)^{1/n} + \left(\frac{w}{c^2}\cos^2\theta\right)^{1/n} \right\}^{n+1}}\,\sqrt{t}(1+t)\,\frac{1-\left(\frac{a^2}{b^2}\right)^{1/e} t^{\frac{1}{e}-1}}{\left\{ 1 + \left(\frac{a^2}{b^2}t\right)^{1/e} \right\}^{e+1}} \tag{A30}$$

$\partial r/\partial\phi$ is regular for all values of θ. $\partial r/\partial\theta$ is also regular for all θ, provided that $n < 2$. Further, it is straightforward to show that the term dependent on $t = \tan^2\phi$ approaches 0 as $t \to \infty$ provided that $e < 2$. Thus, for convex particles ($0 < n, e < 2$) the partial derivatives of r are regular for all values of θ and ϕ.

The surface parameterisations derived here, as well as their partial derivatives, have been implemented into the most recent version of the Tsym program.

References

Adachi, K., & Buseck, P. R. (2015). Changes in shape and composition of sea-salt particles upon aging in an urban atmosphere. *Atmos. Environ.*, *100*, 1 - 9. doi: 10.1016/j.atmosenv.2014.10.036

Barber, C. B., Dobkin, D. P., & Huhdanpaa, H. (1996). The quickhull algorithm for convex hulls. *ACM Trans. Math. Softw.*, *22*(4), 469–483. doi: 10.1145/235815.235821

Barr, A. H. (1981). Superquadrics and angle-preserving transformations. *IEEE Comput. Graphics Appl.*, *1*(1), 11-23. doi: 10.1109/MCG.1981.1673799

Bi, L., Lin, W., Liu, D., & Zhang, K. (2018). Assessing the depolarization capabilities of nonspherical particles in a super-ellipsoidal shape space. *Opt. Express*, *26*(2), 1726–1742. doi: 10.1364/OE.26.001726

Bi, L., Lin, W., Wang, Z., Tang, X., Zhang, X., & Yi, B. (2018). Optical modeling of sea salt aerosols: The effects of nonsphericity and inhomogeneity. *J. Geophys. Res.*, *123*(1), 543-558. Retrieved from `https://agupubs.onlinelibrary.wiley.com/doi/abs/10.1002/2017JD027869` doi: 10.1002/2017JD027869

Bohlmann, S., Baars, H., Radenz, M., Engelmann, R., & Macke, A. (2018). Shipborne aerosol profiling with lidar over the atlantic ocean: from pure marine conditions to complex dust–smoke mixtures. *Atmos. Chem. Phys.*, *18*(13), 9661–9679. Retrieved from https://www.atmos-chem-phys.net/18/9661/2018/ doi: 10.5194/acp-18-9661-2018

Boucher, O. (2015). *Atmospheric aerosols - properties and climate impacts*. Springer, Dordrecht. doi: 10.1007/978-94-017-9649-1

Buseck, P. R., & Pósfai, M. (1999). Airborne minerals and related aerosol particles: Effects on climate and the environment. *Proceedings of the National Academy of Sciences of the United States of America*, *96*(7), 3372–3379.

Carrillo, J., Guerra, J. C., Cuevas, E., & Barrancos, J. (2016, Feb 01). Characterization of the marine boundary layer and the trade-wind inversion over the sub-tropical north atlantic. *Boundary Layer Meteorol.*, *158*(2), 311-330. Retrieved from https://doi.org/10.1007/s10546-015-0081-1 doi: 10.1007/s10546-015-0081-1

Chamaillard, K., Kleefeld, C., Jennings, S., Ceburnis, D., & O'Dowd, C. (2006). Light scattering properties of sea-salt aerosol particles inferred from modeling studies and ground-based measurements. *J. Quant. Spectrosc. Radiat. Transfer*, *101*(3), 498 - 511. Retrieved from http://www.sciencedirect.com/science/article/pii/S0022407306000616 (Light in Planetary Atmospheres and Other Particulate Media) doi: https://doi.org/10.1016/j.jqsrt.2006.02.062

Chi, J. W., Li, W. J., Zhang, D. Z., Zhang, J. C., Lin, Y. T., Shen, X. J., ... Wang, W. X. (2015). Sea salt aerosols as a reactive surface for inorganic and organic acidic gases in the arctic troposphere. *Atmos. Chem. Phys.*, *15*(19), 11341–11353. Retrieved from https://www.atmos-chem-phys.net/15/11341/2015/ doi: 10.5194/acp-15-11341-2015

Cooper, D., Davis, J., & Byers, R. (1974). Measurements of depolarization by dry and humidified salt aerosols using a lidar analogue. *J. Aerosol Sci.*, *5*(2), 117 - 123. Retrieved from http://www.sciencedirect.com/science/article/pii/0021850274900433 doi: https://doi.org/10.1016/0021-8502(74)90043-3

Cotterell, M. I., Willoughby, R. E., Bzdek, B. R., Orr-Ewing, A. J., & Reid, J. P. (2017). A complete parameterisation of the relative humidity and wavelength dependence of the refractive index of hygroscopic inorganic aerosol particles. *Atmos. Chem. Phys.*, *17*(16), 9837–9851. Retrieved from https://www.atmos-chem-phys.net/17/9837/2017/ doi: 10.5194/acp-17-9837-2017

David, G., Thomas, B., Nousiainen, T., Miffre, A., & Rairoux, P. (2013). Retrieving simulated volcanic, desert dust and sea-salt particle properties from two/three-component particle mixtures using uv-vis polarization lidar and t matrix. *Atmos. Chem. Phys.*, *13*, 6757–6776. doi: 10.5194/acp-13-6757-2013

Eldridge, J., & Palik, E. D. (1997). - sodium chloride (nacl). In E. D. Palik (Ed.), *Handbook of optical constants of solids* (p. 775 - 793). Burlington: Academic Press. Retrieved from http://www.sciencedirect.com/science/article/pii/B9780125444156500418 doi: https://doi.org/10.1016/B978-012544415-6.50041-8

Eloranta, E. E. (2005). High spectral resolution lidar. In C. Weitkamp (Ed.), *Lidar: Range-resolved optical remote sensing of the atmosphere* (pp. 143–163). New York, NY: Springer New York. Retrieved from https://doi.org/10.1007/0-387-25101-4_5 doi: 10.1007/0-387-25101-4_5

Foltescu, V., Pryor, S. C., & Bennet, C. (2005). Sea salt generation, dispersion and removal on the regional scale. *Atmos. Environ.*, *39*, 2123-2133.

Gasteiger, J., Wiegner, M., Groß, S., Freudenthaler, V., Toledano, C., Tesche, M., & Kandler, K. (2011). Modelling lidar-relevant optical properties of complex mineral dust aerosols. *Tellus B*, *63*(4), 725–741. doi: 10.1111/j.1600-0889.2011.00559.x

Groß, S., Esselborn, M., Weinzierl, B., Wirth, M., Fix, A., & Petzold, A. (2013). Aerosol classification by airborne high spectral resolution lidar observations. *Atmos. Chem. Phys.*, *13*(5), 2487–2505. doi: 10.5194/acp-13-2487-2013

Gwaze, P., Helas, G. A., Annegarn, H. J., Huth, J., & Piketh, S. J. (2007). Physical, chemical and optical properties of aerosol particles collected over Cape Town during winter haze episodes. *S. Afr. J. Sci.*, *103*, 35 - 43. Retrieved from http://www.scielo.org.za/scielo.php?script=sci_arttext&pid=S0038-23532007000100010&nrm=iso

Haarig, M., Ansmann, A., Gasteiger, J., Kandler, K., Althausen, D., Baars, H., ... Farrell, D. A. (2017). Dry versus wet marine particle optical properties: Rh dependence of depolarization ratio, backscatter, and extinction from multi-wavelength lidar measurements during saltrace. *Atmos. Chem. Phys.*, *17*(23), 14199–14217. doi: 10.5194/acp-17-14199-2017

Hänel, G. (1976). The properties of atmospheric aerosol particles as functions of the relative humidity at thermodynamic equilibrium with the surrounding moist air. In H. Landsberg & J. V. Mieghem (Eds.), (Vol. 19, p. 73 - 188). Elsevier. Retrieved from http://www.sciencedirect.com/science/article/pii/S0065268708601429 doi: https://doi.org/10.1016/S0065-2687(08)60142-9

Irshad, R., Grainger, R. G., Peters, D. M., McPheat, R. A., Smith, K. M., & Thomas, G. (2009). Laboratory measurements of the optical properties of sea salt aerosol. *Atmos. Chem. Phys.*, *9*(1), 221–230. Retrieved from https://www.atmos-chem-phys.net/9/221/2009/ doi: 10.5194/acp-9-221-2009

Järvinen, E., Kemppinen, O., Nousiainen, T., Kociok, T., Möhler, O., Leisner, T., & Schnaiter, M. (2016). Laboratory investigations of mineral dust near-backscattering depolarization ratios. *J. Quant. Spectrosc. Radiat. Transfer*, *178*, 192 - 208. Retrieved from http://www.sciencedirect.com/science/article/pii/S0022407315301722 (Electromagnetic and light scattering by nonspherical particles XV: Celebrating 150 years of Maxwell's electromagnetics) doi: https://doi.org/10.1016/j.jqsrt.2016.02.003

Kahnert, M. (2005). Irreducible representations of finite groups in the T matrix formulation of the electromagnetic scattering problem. *J. Opt. Soc. Am. A*, *22*, 1187-1199.

Kahnert, M. (2013). The T-matrix code Tsym for homogeneous dielectric particles with finite symmetries. *J. Quant. Spectrosc. Radiat. Transfer*, *123*, 62-78.

Kahnert, M., Kanngießer, F., Järvinen, E., & Schnaiter, M. (2020). Aerosol-optics model for the backscatter depolarisation ratio of mineral dust particles. *J. Quant. Spectrosc. Radiat. Transfer*, *254*, 107177. Retrieved from http://www.sciencedirect.com/science/article/pii/S0022407320303502 doi: https://doi.org/10.1016/j.jqsrt.2020.107177

Kahnert, M., & Kanngießer, F. (2020). Modelling optical properties of atmospheric black carbon aerosols. *J. Quant. Spectrosc. Radiat. Transfer*, *244*, 106849. Retrieved from http://www.sciencedirect.com/science/article/pii/S0022407319309550 doi: https://doi.org/10.1016/j.jqsrt.2020.106849

King, S. M., Butcher, A. C., Rosenoern, T., Coz, E., Lieke, K. I., de Leeuw, G., ... Bilde, M. (2012, 02). Investigating primary marine aerosol properties: Ccn activity of sea salt and mixed inorganic-organic particles. *Environ. Sci. Technol.*, *46*(19), 10405-10412. Retrieved from https://doi.org/10.1021/es300574u doi: 10.1021/es300574u

Krishnamurti, T. N., Stefanova, L., & vasubandhu Misra. (2013). *Tropical meteorology: An introduction*. New York, NY: Springer New York. doi: 10.1007/978-1-4614-7409-8

McInnes, L. M., Covert, D. S., Quinn, P. K., & Germani, M. S. (1994). Measurements of chloride depletion and sulfur enrichment in individual sea-salt particles collected from the remote marine boundary layer. *Journal of Geophysical Research: Atmospheres*, *99*(D4), 8257-8268. doi: 10.1029/93JD03453

Meira, G., Andrade, C., Alonso, C., Padaratz, I., & Borba, J. (2008). Modelling sea-salt transport and deposition in marine atmosphere zone – a tool for corrosion studies. *Corros. Sci.*, *50*(9), 2724 - 2731. Retrieved from http://www.sciencedirect.com/science/article/pii/S0010938X08002333 doi: https://doi.org/10.1016/j.corsci.2008.06.028

Mishchenko, M. I., & Hovenier, J. W. (1995). Depolarization of light backscattered by randomly oriented nonspherical particles. *Opt. Lett.*, *20*(12), 1356–1358. doi: 10.1364/OL.20.001356

Mishchenko, M. I., Travis, L. D., & Lacis, A. A. (2002). *Scattering, absorption, and emission of light by small particles.* CAMBRIDGE UNIVERSITY PRESS.

Muinonen, K., Nousiainen, T., Fast, P., Lumme, K., & Peltoniemi, J. (1996). Light scattering by gaussian random particles: Ray optics approximation. *J. Quant. Spectrosc. Radiat. Transfer*, *55*(5), 577 - 601. Retrieved from http://www.sciencedirect.com/science/article/pii/0022407396000039 (Light Scattering by Non-Spherical Particles) doi: 10.1016/0022-4073(96)00003-9

Murayama, T. H., Okamoto, H., Kaneyasu, N., Kamataki, H., & Miura, K. (1999). Application of lidar depolarization measurement in the atmospheric boundary layer: Effects of dust and sea-salt particles. *J. Geophys. Res.*, *104*(D24), 31781-31792. Retrieved from https://agupubs.onlinelibrary.wiley.com/doi/abs/10.1029/1999JD900503 doi: 10.1029/1999JD900503

Murphy, D. M., Anderson, J. R., Quinn, P. K., McInnes, L. M., Brechtel, F. J., Kreidenweis, S. M., ... Buseck, P. R. (1998, Mar 01). Influence of sea-salt on aerosol radiative properties in the southern ocean marine boundary layer. *Nature*, *392*(6671), 62-65. Retrieved from https://doi.org/10.1038/32138 doi: 10.1038/32138

Nousiainen, T., & Kandler, K. (2015). Light scattering by atmospheric mineral dust particles. In A. A. Kokhanovsky (Ed.), *Light scattering reviews 9: Light scattering and radiative transfer* (pp. 3–52). Berlin, Heidelberg: Springer Berlin Heidelberg. Retrieved from https://doi.org/10.1007/978-3-642-37985-7_1 doi: 10.1007/978-3-642-37985-7_1

Patterson, J. P., Collins, D. B., Michaud, J. M., Axson, J. L., Sultana, C. M., Moser, T., ... Gianneschi, N. C. (2016, 27). Sea spray aerosol structure and composition using cryogenic transmission electron microscopy. *ACS Cent. Sci.*, *2*(1), 40-47. Retrieved from https://doi.org/10.1021/acscentsci.5b00344 doi: 10.1021/acscentsci.5b00344

Peart, A., & Evans, J. R. G. (2011). Study of sea salt particles launched by bubble burst. *Bub. Sci. Eng. Technol.*, *3*(2), 64-72. Retrieved from https://www.tandfonline.com/doi/abs/10.1179/1758897911Y.0000000004 doi: 10.1179/1758897911Y.0000000004

Porter, J. N., & Clarke, A. D. (1997). Aerosol size distribution models based on in situ measurements. *J. Geophys. Res.*, *109*, 6035–6045.

Pósfai, M., Anderson, J. R., Buseck, P. R., & Sievering, H. (1995). Compositional variations of sea-salt-mode aerosol particles from the north atlantic. *J. Geophys. Res.*, *100*(D11), 23063-23074. Retrieved from https://agupubs.onlinelibrary.wiley.com/doi/abs/10.1029/95JD01636 doi: 10.1029/95JD01636

Sakai, T., Nagai, T., Mano, Y., Zaizen, Y., & Inomata, Y. (2012). Aerosol optical and microphysical properties as derived from collocated measurements using polarization lidar and direct sampling. *Atmos. Environ.*, *60*, 419 - 427. Retrieved from http://www.sciencedirect.com/science/article/pii/S1352231012006528 doi: https://doi.org/10.1016/j.atmosenv.2012.06.068

Sakai, T., Nagai, T., Zaizen, Y., & Mano, Y. (2010). Backscattering linear depolarization ratio measurements of mineral, sea-salt, and ammonium sulfate particles simulated in a laboratory chamber. *Appl. Opt.*, *49*(23), 4441–4449. Retrieved from http://ao.osa.org/abstract.cfm?URI=ao-49-23-4441 doi:

10.1364/AO.49.004441

Sakai, T., Shibata, T., Kwon, S.-A., Kim, Y.-S., Tamura, K., & Iwasaka, Y. (2000). Free tropospheric aerosol backscatter, depolarization ratio, and relative humidity measured with the raman lidar at nagoya in 1994–1997: contributions of aerosols from the asian continent and the pacific ocean. *Atmos. Environ.*, *34*(3), 431 - 442. Retrieved from http://www.sciencedirect.com/science/article/pii/S1352231099003283 doi: https://doi.org/10.1016/S1352-2310(99)00328-3

Schulz, F. M., Stamnes, K., & Stamnes, J. J. (1999). Point group symmetries in electromagnetic scattering. *J. Opt. Soc. Am. A*, *16*, 853-865.

Shettle, E. P., & Fenn, R. W. (1979). *Models for the aerosols of the lower atmosphere and the effects of humidity variations on their optical properties* (AFGL Technical Report No. AFGL-TR-79–021A). Air Force Geophysics Laboratory. Retrieved from https://apps.dtic.mil/docs/citations/ADA08595

Tang, I. N., Tridico, A. C., & Fung, K. H. (1997). Thermodynamic and optical properties of sea salt aerosols. *Journal of Geophysical Research: Atmospheres*, *102*(D19), 23269-23275. Retrieved from https://agupubs.onlinelibrary.wiley.com/doi/abs/10.1029/97JD01806 doi: 10.1029/97JD01806

Torge, A., Macke, A., Heinold, B., & Wauer, J. (2011). Solar radiative transfer simulations in saharan dust plumes: particle shapes and 3-d effect. *Tellus B*, *63*(4), 770-780. Retrieved from https://onlinelibrary.wiley.com/doi/abs/10.1111/j.1600-0889.2011.00560.x doi: 10.1111/j.1600-0889.2011.00560.x

Ueda, S., Hirose, Y., Miura, K., & Okochi, H. (2014). Individual aerosol particles in and below clouds along a mt. fuji slope: Modification of sea-salt-containing particles by in-cloud processing. *Atmos. Res.*, *137*, 216 - 227. Retrieved from http://www.sciencedirect.com/science/article/pii/S0169809513002846 doi: https://doi.org/10.1016/j.atmosres.2013.10.011

Virtanen, P., Gommers, R., Oliphant, T. E., Haberland, M., Reddy, T., Cournapeau, D., ... SciPy 1.0 Contributors (2020, Mar 01). Scipy 1.0: fundamental algorithms for scientific computing in python. *Nature Methods*, *17*(3), 261-272. Retrieved from https://doi.org/10.1038/s41592-019-0686-2 doi: 10.1038/s41592-019-0686-2

Wandinger, U. (2005). Raman lidar. In C. Weitkamp (Ed.), *Lidar: Range-resolved optical remote sensing of the atmosphere* (pp. 241–271). New York, NY: Springer New York. Retrieved from https://doi.org/10.1007/0-387-25101-4_9 doi: 10.1007/0-387-25101-4_9

Wang, Z., Bi, L., Yi, B., & Zhang, X. (2019). How the inhomogeneity of wet sea salt aerosols affects direct radiative forcing. *Geophys. Res. Lett.*, *46*(3), 1805-1813. Retrieved from https://agupubs.onlinelibrary.wiley.com/doi/abs/10.1029/2018GL081193 doi: 10.1029/2018GL081193

Wells, N. C. (2011). *The atmosphere and ocean: A physical introduction* (3rd Edition ed.). John Wiley & Sons, Inc.

Wise, M. E., Biskos, G., Martin, S. T., Russell, L. M., & Buseck, P. R. (2005). Phase transitions of single salt particles studied using a transmission electron microscope with an environmental cell. *Aerosol Sci. Technol.*, *39*(9), 849-856. Retrieved from https://doi.org/10.1080/02786820500295263 doi: 10.1080/02786820500295263

Wriedt, T. (2002). Using the t-matrix method for light scattering computations by non-axisymmetric particles: Superellipsoids and realistically shaped particles. *Part. Part. Sys. Charact.*, *19*(4), 256-268. doi: 10.1002/1521-4117(200208)19:4⟨256::AID-PPSC256⟩3.0.CO;2-8

Yin, Z., Ansmann, A., Baars, H., Seifert, P., Engelmann, R., Radenz, M., ... Maupin, F. (2019). Aerosol measurements with a shipborne sun–sky–lunar photometer and collocated multiwavelength raman polarization lidar over the atlantic ocean. *Atmos. Meas. Tech.*, *12*(10), 5685–5698. Re-

trieved from https://www.atmos-meas-tech.net/12/5685/2019/ doi: 10.5194/amt-12-5685-2019

Yurkin, M. A., & Hoekstra, A. G. (2007). The discrete dipole approximation: An overview and recent developments. *J. Quant. Spectrosc. Radiat. Transfer*, *106*(1), 558–589. (IX Conference on Electromagnetic and Light Scattering by Non-Spherical Particles) doi: 10.1016/j.jqsrt.2007.01.034

Yurkin, M. A., & Hoekstra, A. G. (2011). The discrete-dipole-approximation code adda: Capabilities and known limitations. *J. Quant. Spectrosc. Radiat. Transfer*, *112*(13). doi: 10.1016/j.jqsrt.2011.01.031

Yurkin, M. A., Maltsev, V. P., & Hoekstra, A. G. (2006, Oct). Convergence of the discrete dipole approximation. ii. an extrapolation technique to increase the accuracy. *J. Opt. Soc. Am. A*, *23*(10), 2592–2601. Retrieved from http://josaa.osa.org/abstract.cfm?URI=josaa-23-10-2592 doi: 10.1364/JOSAA.23.002592

Zeng, J., Zhang, G., Long, S., Liu, K., Cao, L., Bao, L., & Li, Y. (2013). Sea salt deliquescence and crystallization in atmosphere: an in situ investigation using x-ray phase contrast imaging. *Surface and Interface Analysis*, *45*(5), 930-936. Retrieved from https://onlinelibrary.wiley.com/doi/abs/10.1002/sia.5184 doi: 10.1002/sia.5184

Zieger, P., Väisänen, O., Corbin, J. C., Partridge, D. G., Bastelberger, S., Mousavi-Fard, M., ... Salter, M. E. (2017). Revising the hygroscopicity of inorganic sea salt particles. *Nat. Commun.*, *8*(1), 15883. doi: 10.1038/ncomms15883

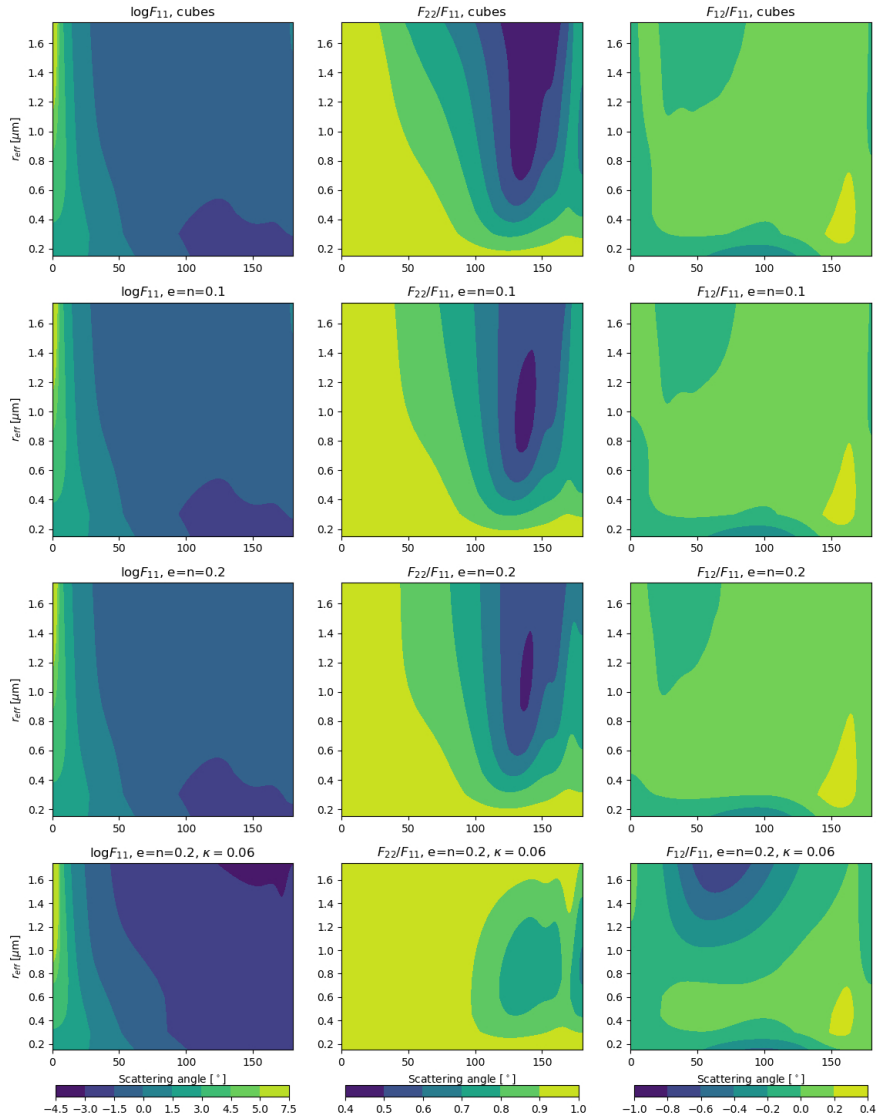

Figure 16. Elements of the Stokes scattering matrix as a function of scattering angle and effective radius r_{eff}. The three columns show the elements $\log F_{11}$ (left), F_{22}/F_{11} (centre), and F_{12}/F_{11} (right). The rows show results for an imaginary part of the refractive index $\kappa = 0$ (rows 1–3), and $\kappa = 0.06$ (row 4), as well as for roundness parameters $e = n = 0$ (rows 1 and 4), $e = n = 0.1$ (row 2), and $e = n = 0.2$ (row 3).

Figure 1.

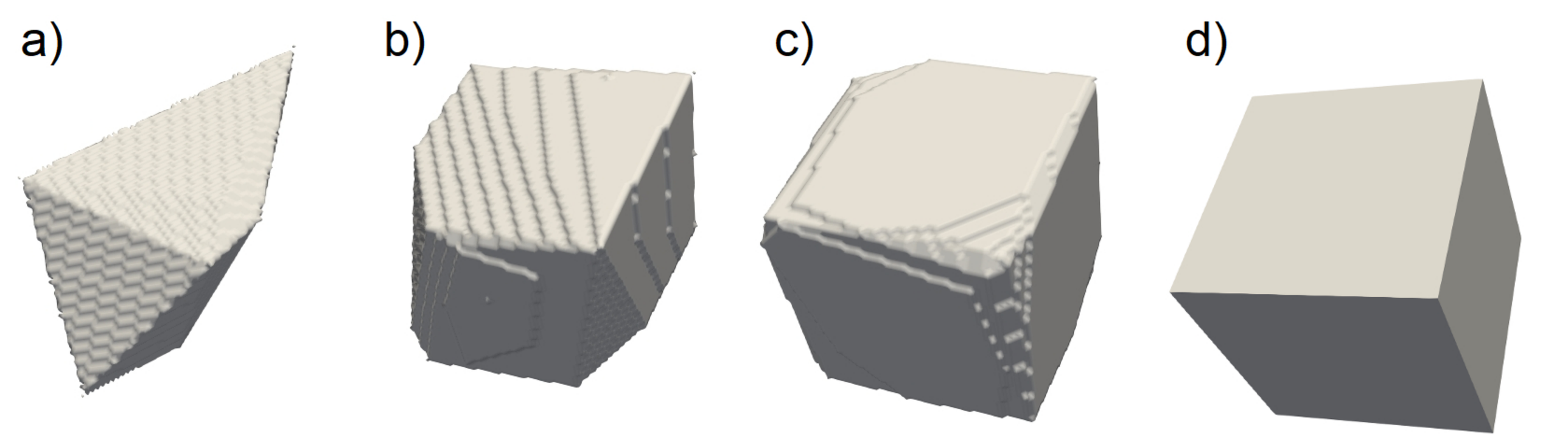
a)
b)
c)
d)

Figure 2.

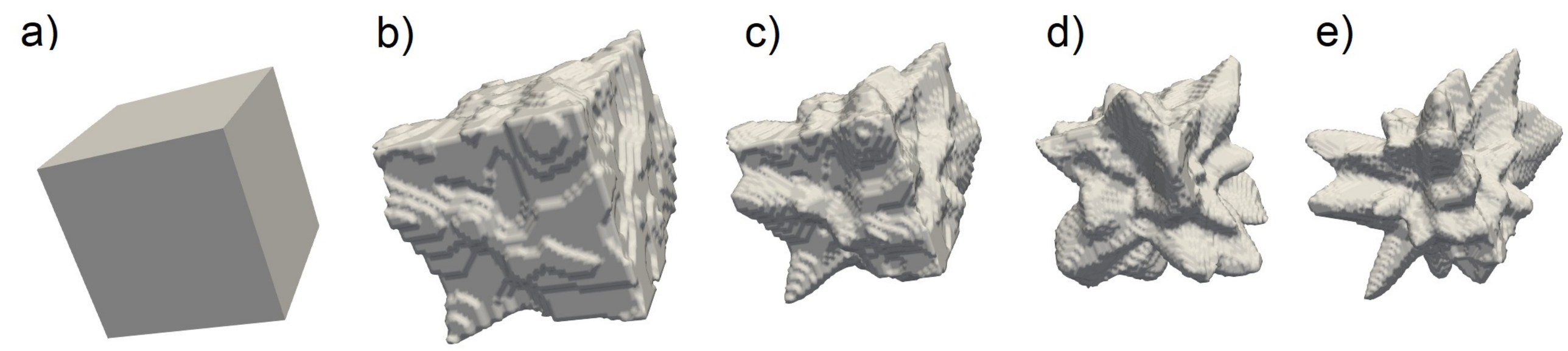
a)
b)
c)
d)
e)

Figure 3.

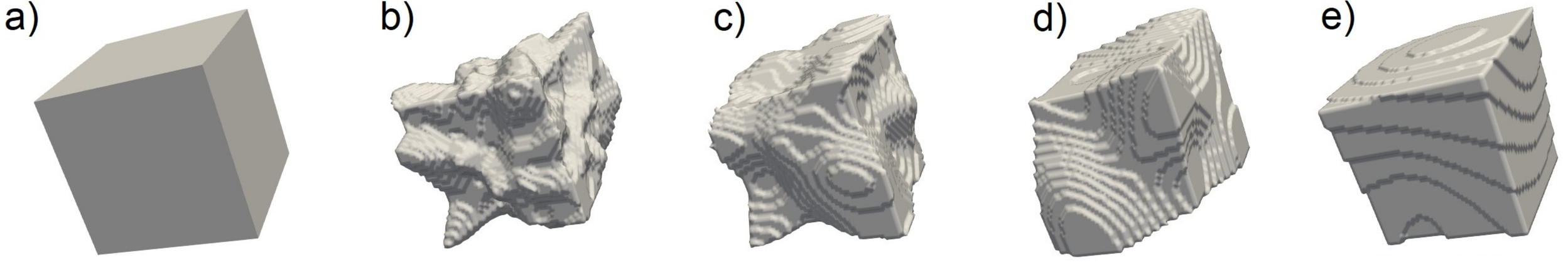
a)
b)
c)
d)
e)

Figure 4.

a)

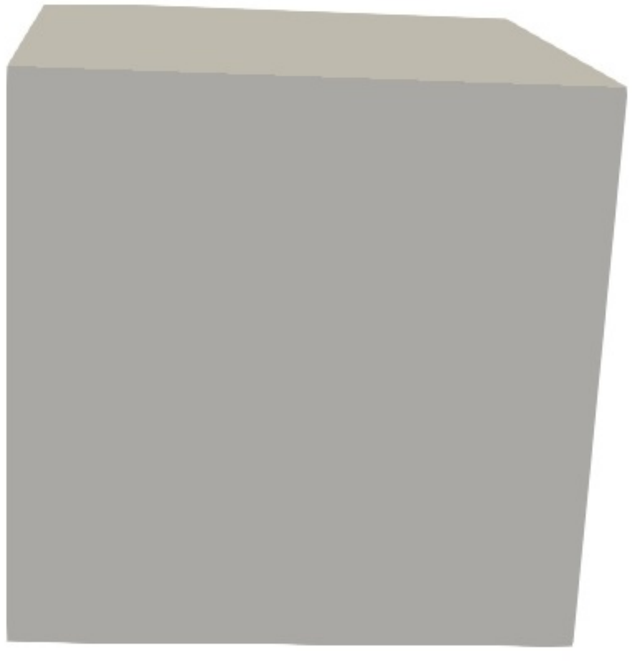

b)

c)

d)

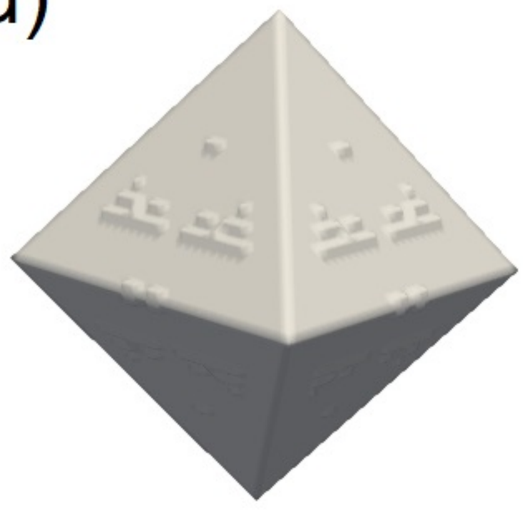

e)

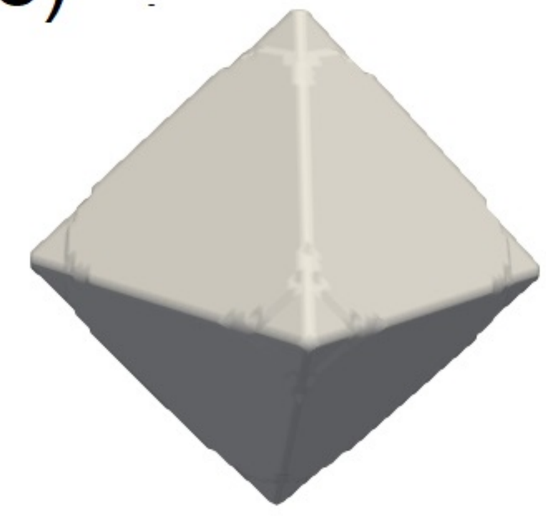

f)

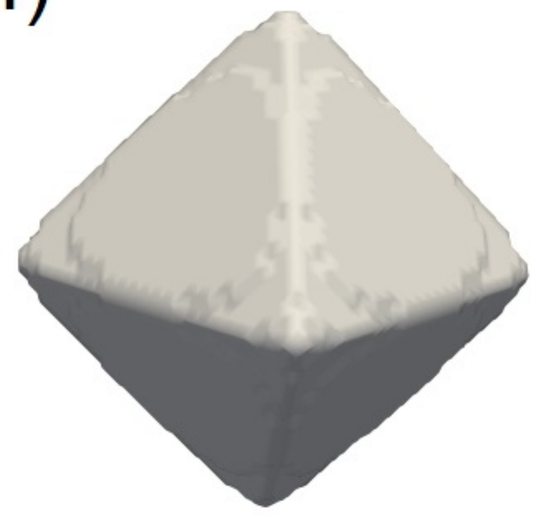

Figure 5.

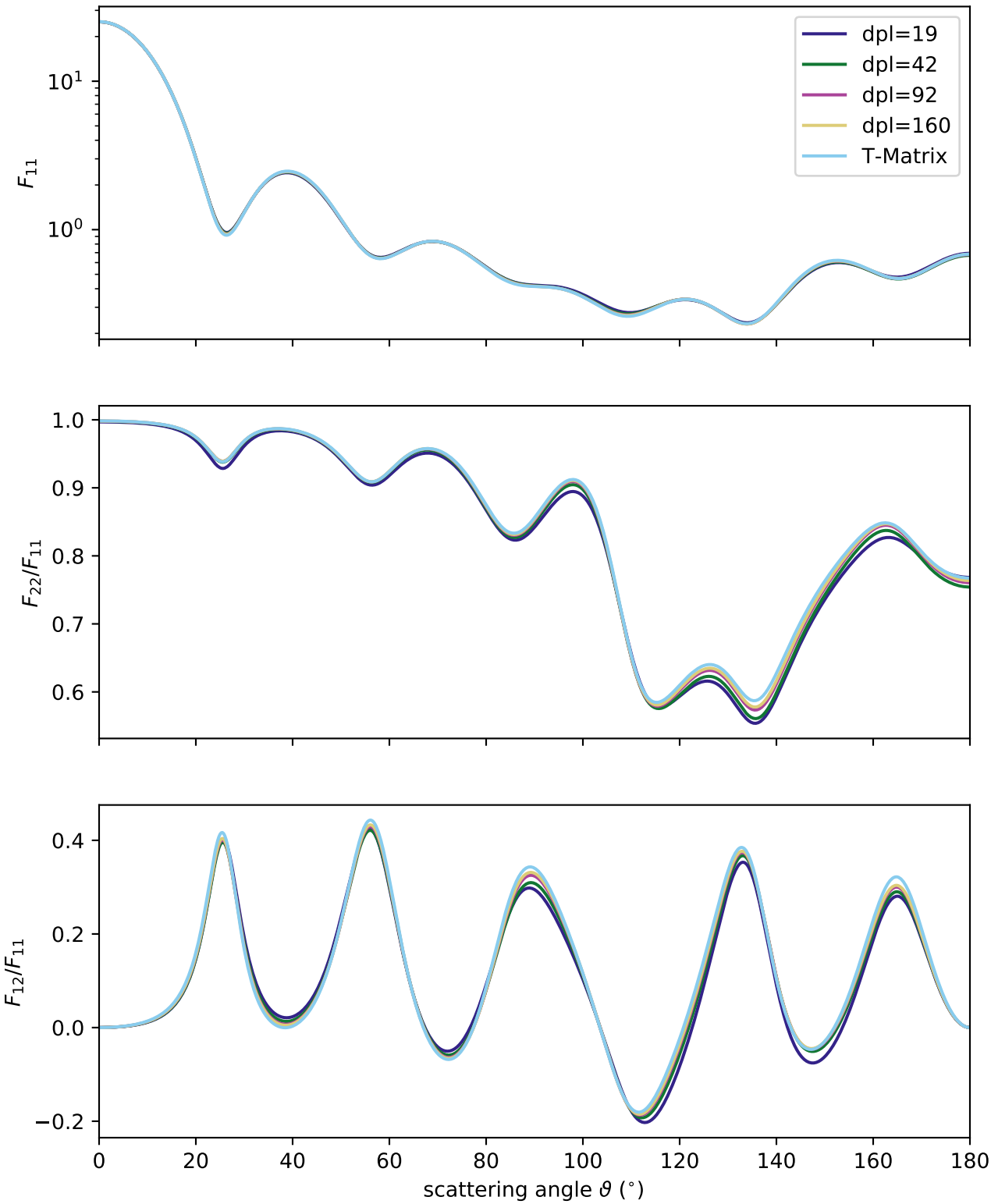
dpl=19
dpl=42
dpl=92
dpl=160
T-Matrix
F_{11}
10^1
10^0
F_{22}/F_{11}
1.0
0.9
0.8
0.7
0.6
F_{12}/F_{11}
0.4
0.2
0.0
−0.2
0
20
40
60
80
100
120
140
160
180
scattering angle ϑ (°)

Figure 6.

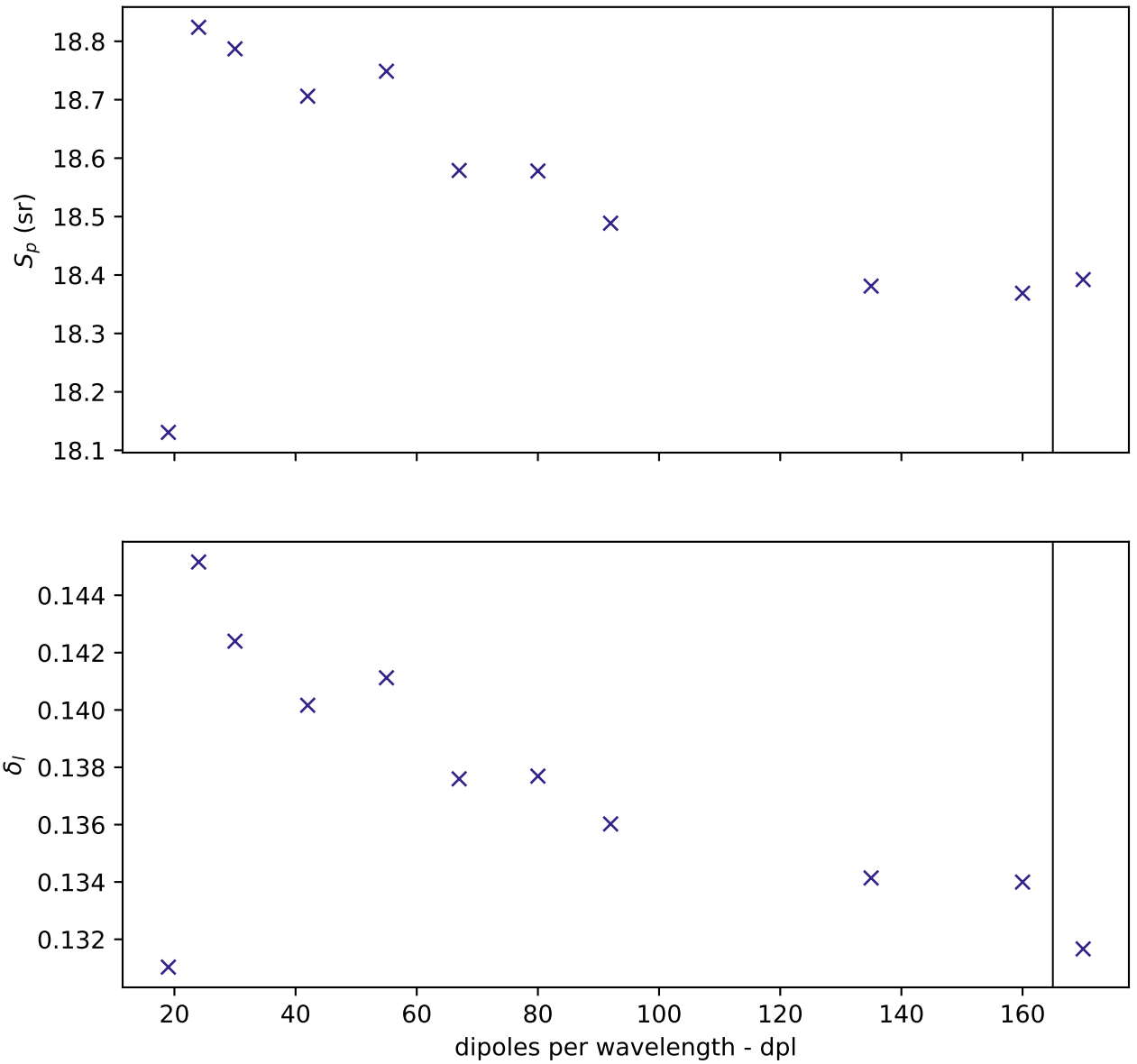
18.8
18.7
18.6
18.5
18.4
18.3
18.2
18.1
S_p (sr)
0.144
0.142
0.140
0.138
0.136
0.134
0.132
δ_l
20
40
60
80
100
120
140
160
dipoles per wavelength - dpl

Figure 7.

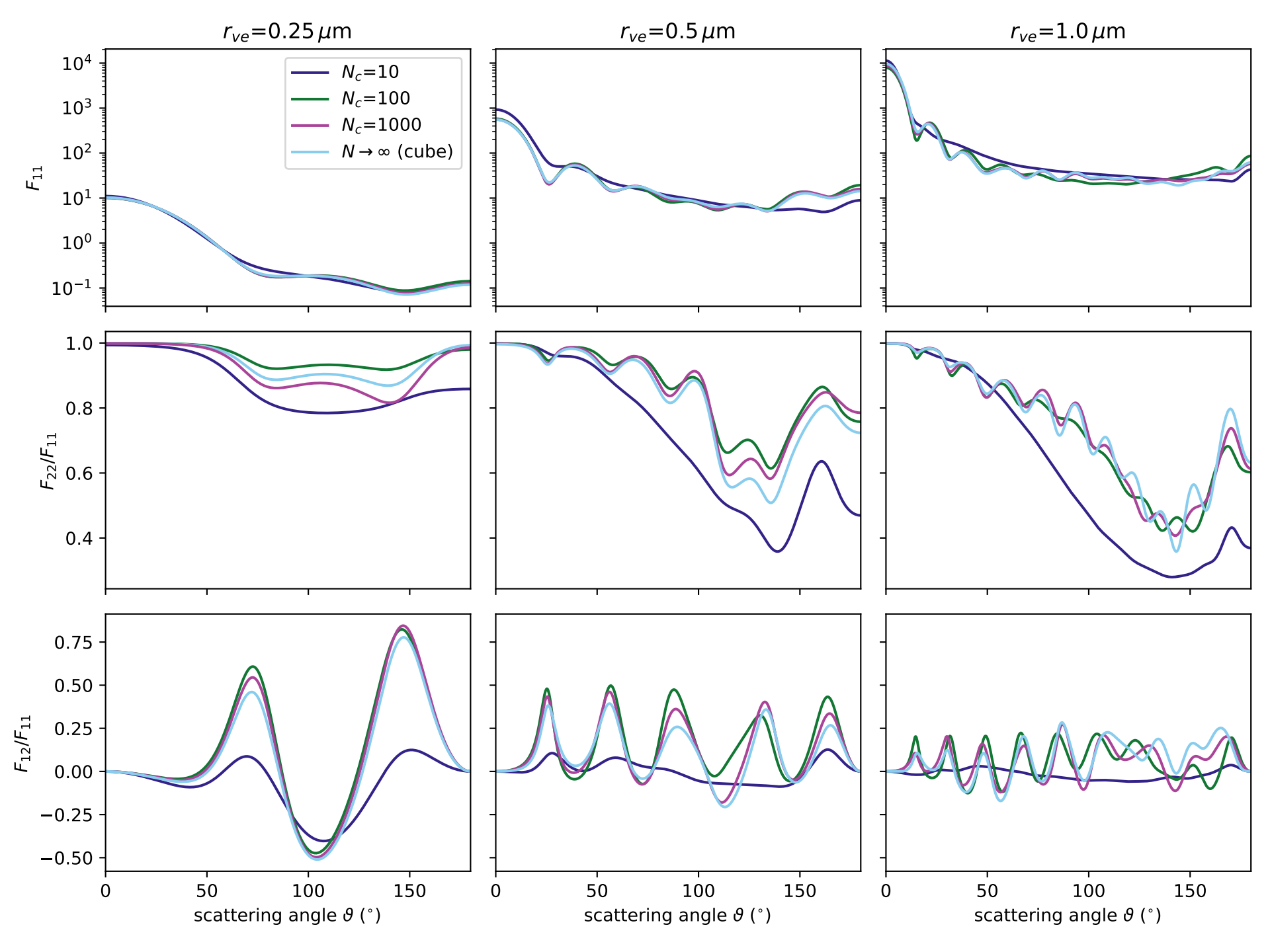
r_{ve}=0.25 μm
r_{ve}=0.5 μm
r_{ve}=1.0 μm
N_c=10
N_c=100
N_c=1000
$N \to \infty$ (cube)
F_{11}
F_{22}/F_{11}
F_{12}/F_{11}
scattering angle ϑ (°)
scattering angle ϑ (°)
scattering angle ϑ (°)

Figure 8.

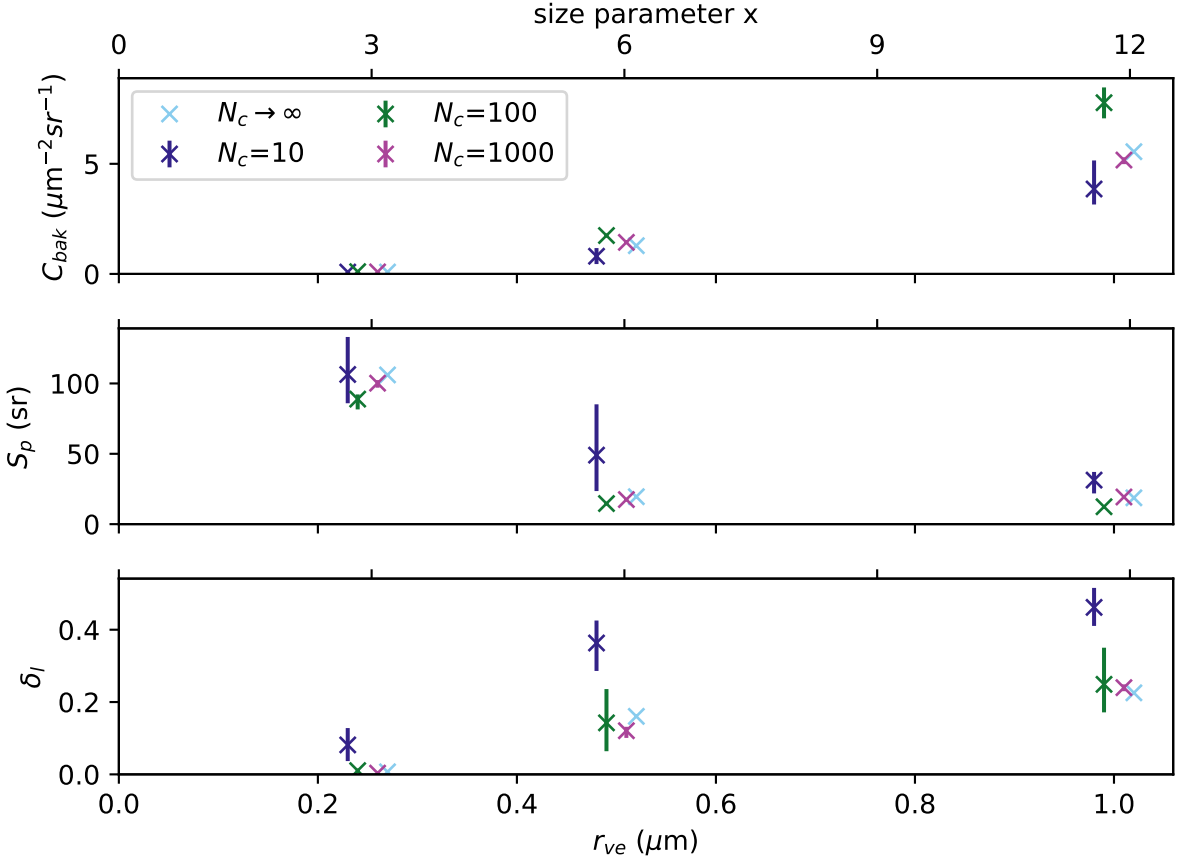
size parameter x
0
3
6
9
12
$N_c \to \infty$
N_c=10
N_c=100
N_c=1000
C_{bak} (μm^{-2}sr^{-1})
0
5
S_p (sr)
0
50
100
δ_l
0.0
0.2
0.4
0.0
0.2
0.4
0.6
0.8
1.0
r_{ve} (μm)

Figure 9.

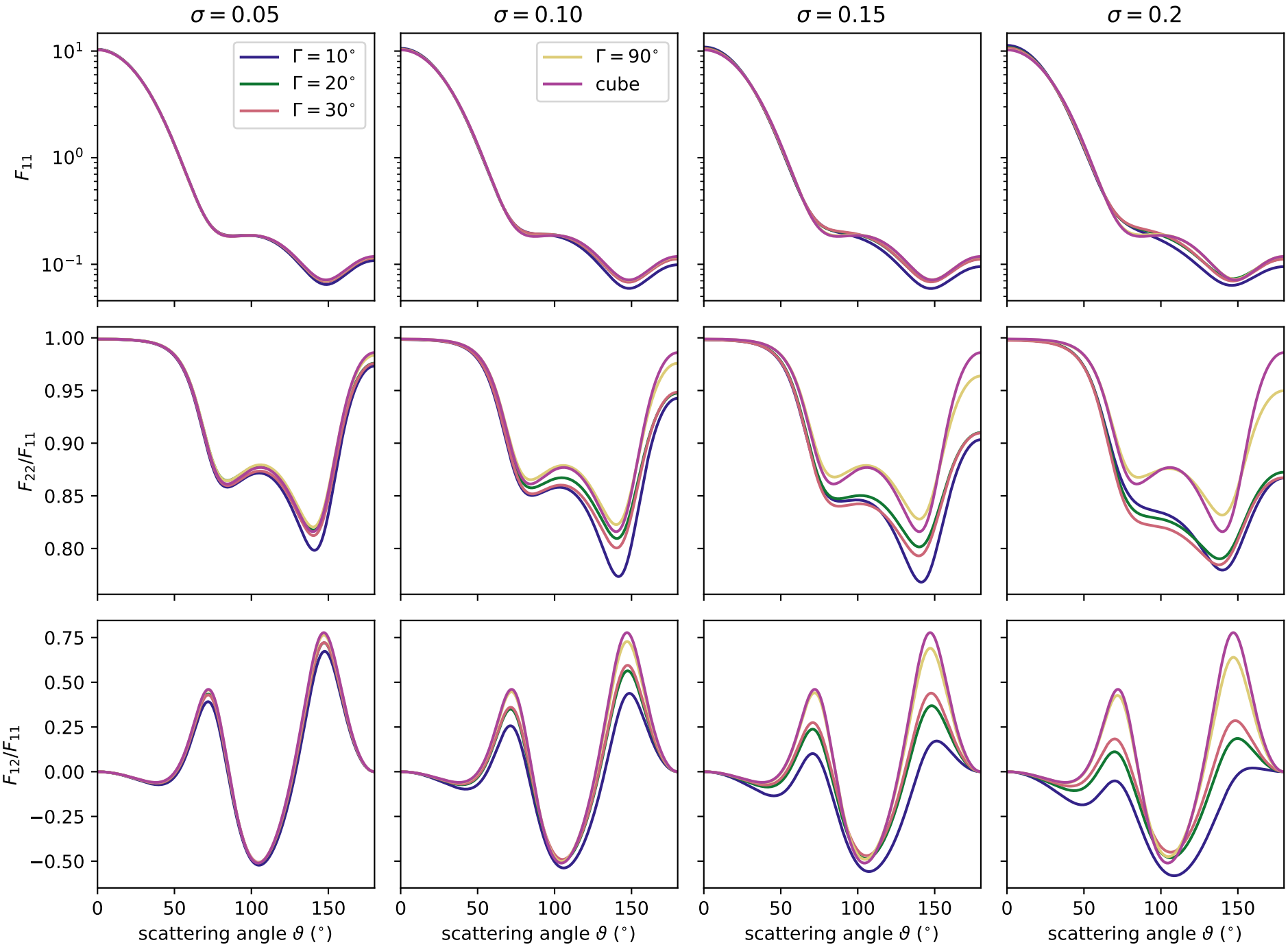
$\sigma = 0.05$
$\sigma = 0.10$
$\sigma = 0.15$
$\sigma = 0.2$
$\Gamma = 10°$
$\Gamma = 20°$
$\Gamma = 30°$
$\Gamma = 90°$
cube
F_{11}
F_{22}/F_{11}
F_{12}/F_{11}
scattering angle ϑ (°)

Figure 10.

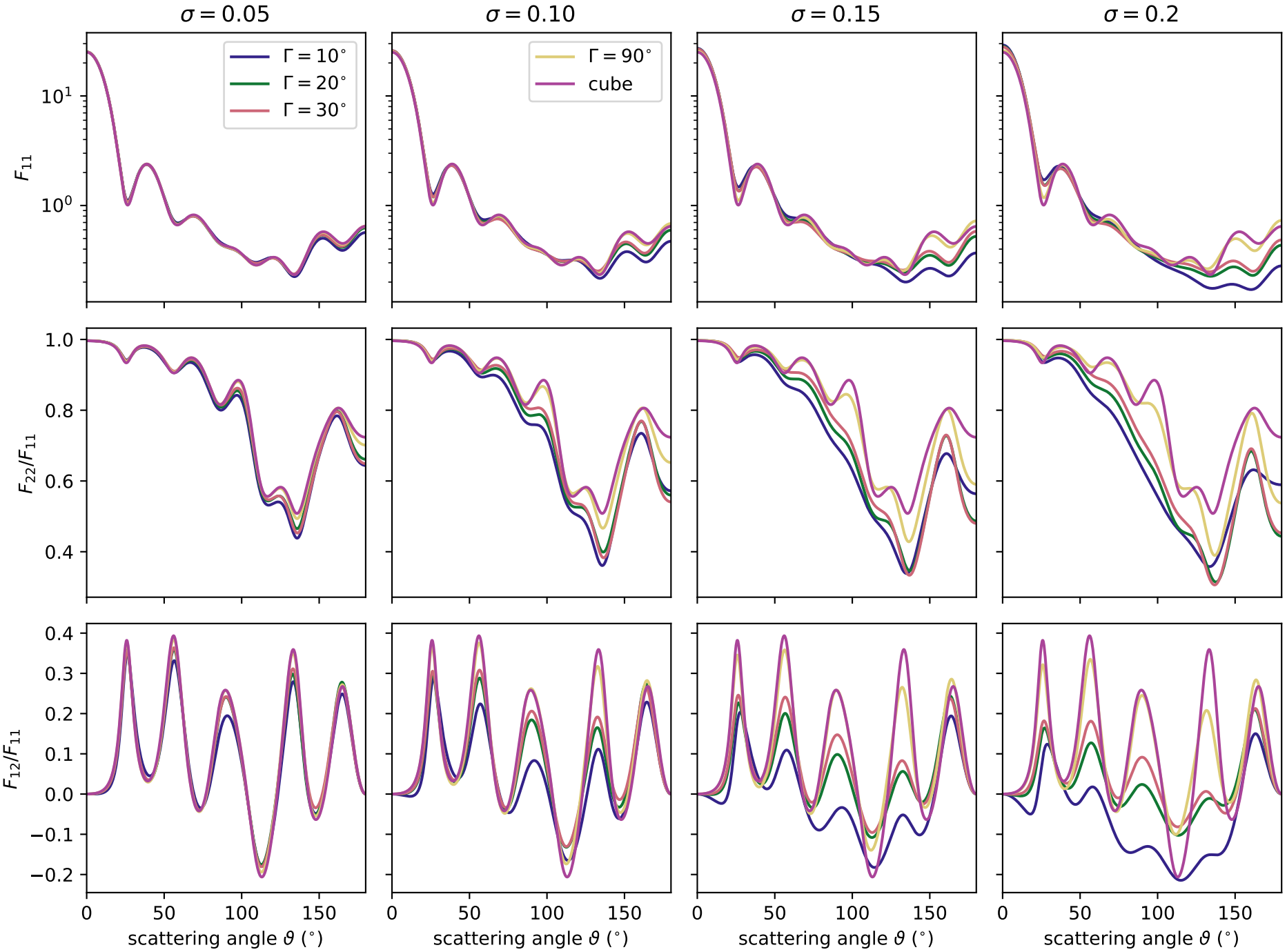
σ = 0.05
σ = 0.10
σ = 0.15
σ = 0.2
Γ = 10°
Γ = 20°
Γ = 30°
Γ = 90°
cube
F11
F22/F11
F12/F11
scattering angle ϑ (°)

Figure 11.

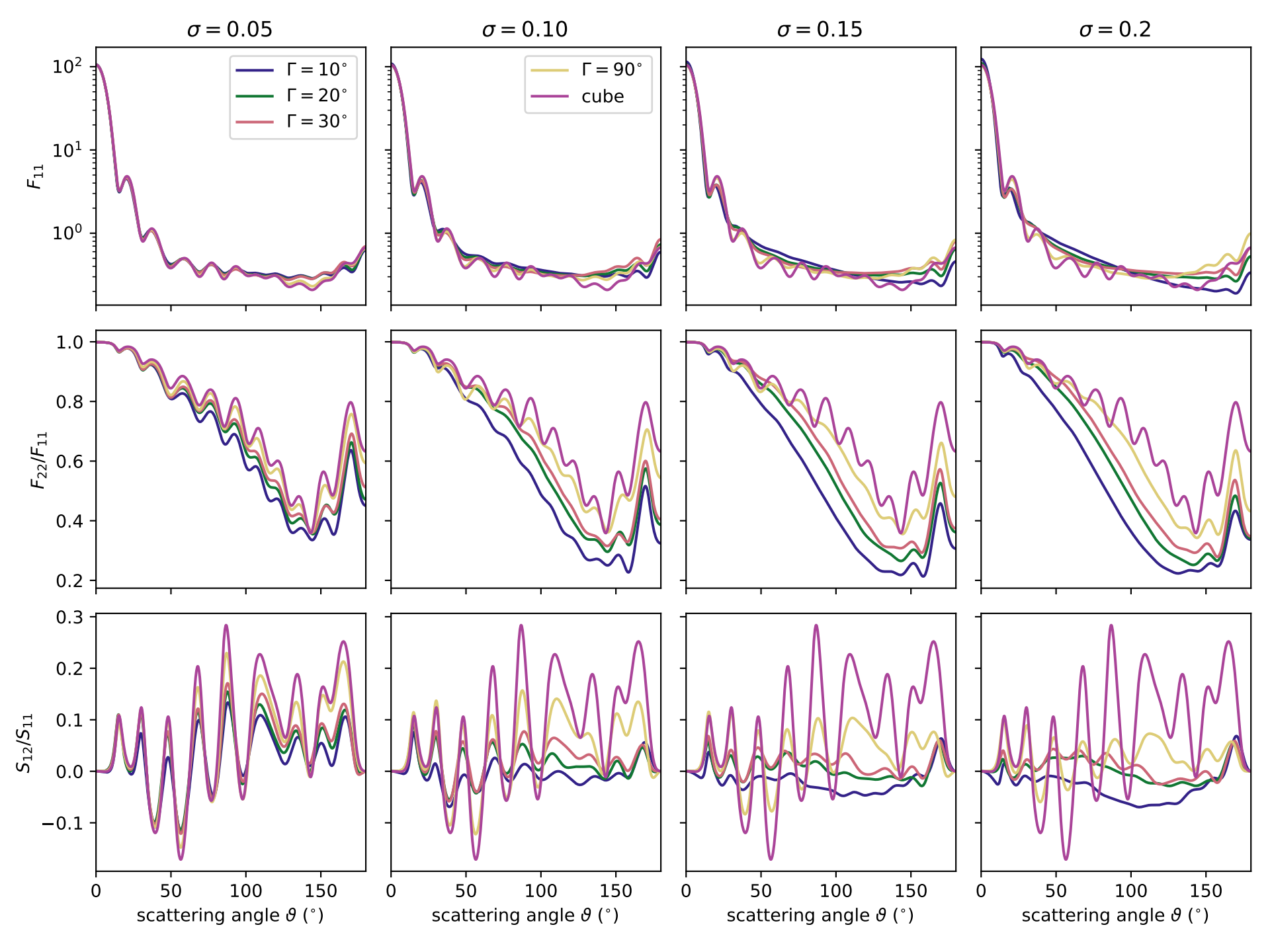
$\sigma = 0.05$
$\sigma = 0.10$
$\sigma = 0.15$
$\sigma = 0.2$
$\Gamma = 10°$
$\Gamma = 20°$
$\Gamma = 30°$
$\Gamma = 90°$
cube
F_{11}
F_{22}/F_{11}
S_{12}/S_{11}
scattering angle ϑ (°)

Figure 12.

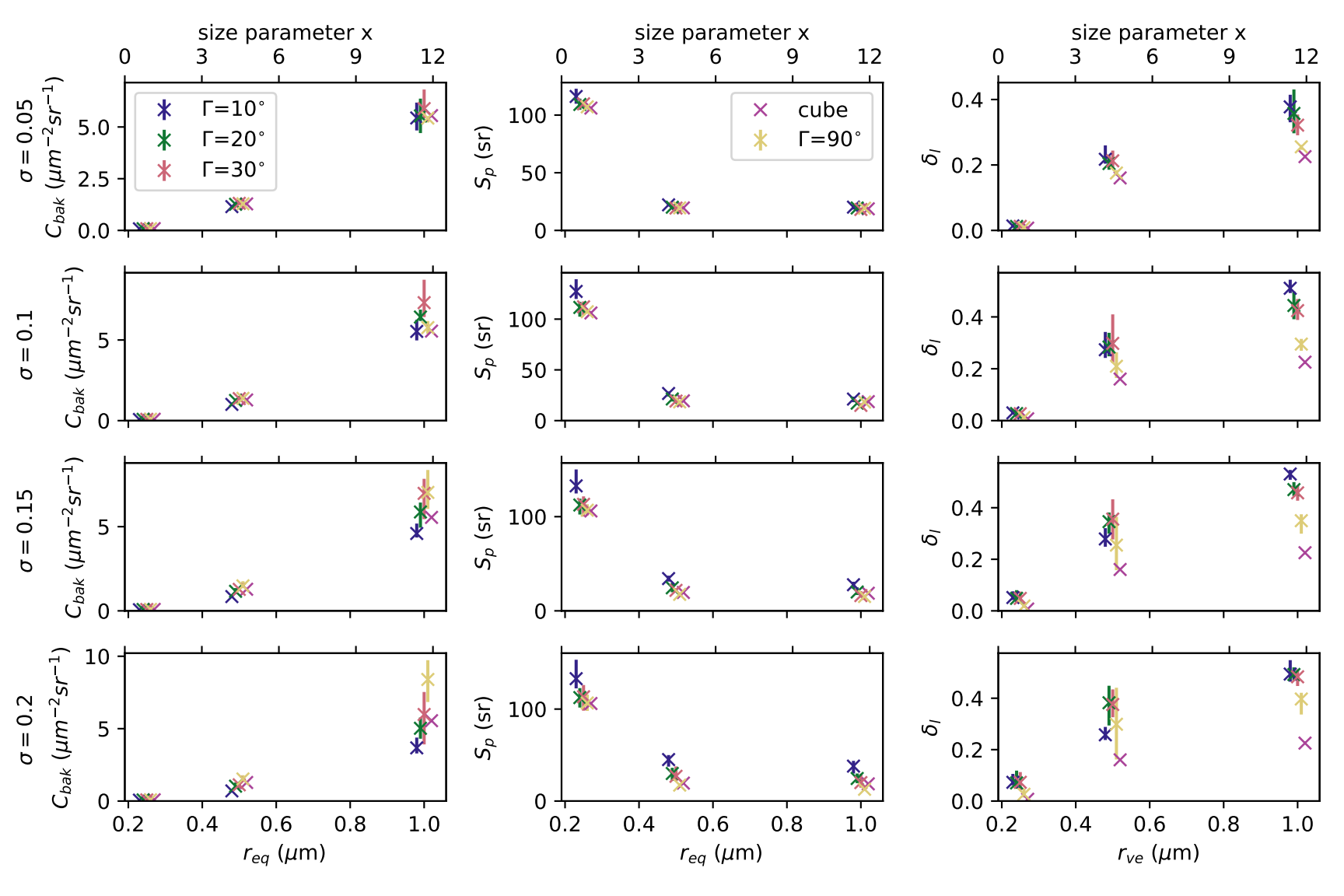
size parameter x
0
3
6
9
12
σ = 0.05
σ = 0.1
σ = 0.15
σ = 0.2
C_{bak} ($\mu m^{-2} sr^{-1}$)
S_p (sr)
δ_l
Γ=10°
Γ=20°
Γ=30°
cube
Γ=90°
r_{eq} (μm)
r_{ve} (μm)

Figure 13.

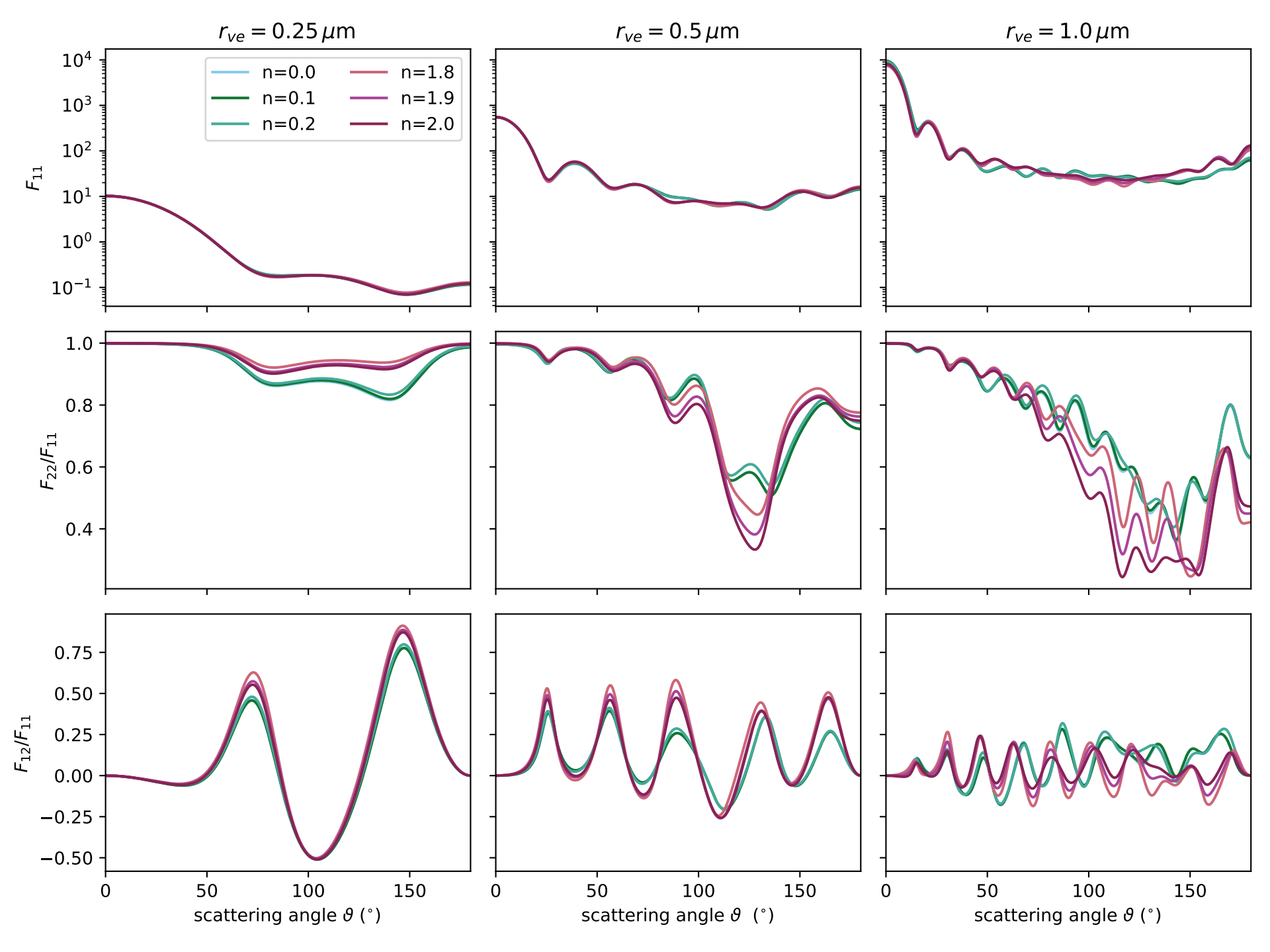
$r_{ve} = 0.25\,\mu m$
$r_{ve} = 0.5\,\mu m$
$r_{ve} = 1.0\,\mu m$
n=0.0
n=0.1
n=0.2
n=1.8
n=1.9
n=2.0
F_{11}
F_{22}/F_{11}
F_{12}/F_{11}
scattering angle ϑ (°)
scattering angle ϑ (°)
scattering angle ϑ (°)

Figure 14.

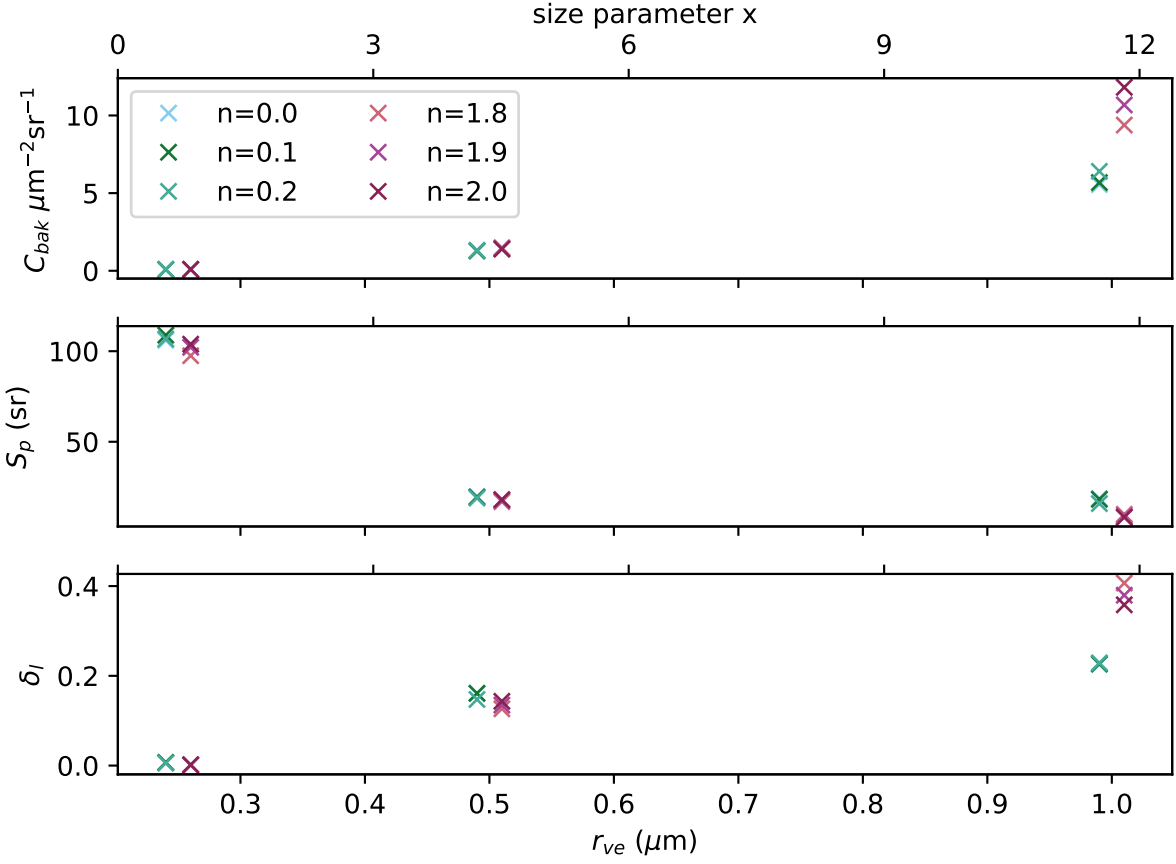
size parameter x
0
3
6
9
12
n=0.0
n=0.1
n=0.2
n=1.8
n=1.9
n=2.0
C_{bak} $\mu m^{-2} sr^{-1}$
0
5
10
S_p (sr)
50
100
δ_l
0.0
0.2
0.4
0.3
0.4
0.5
0.6
0.7
0.8
0.9
1.0
r_{ve} (μm)

Figure 15.

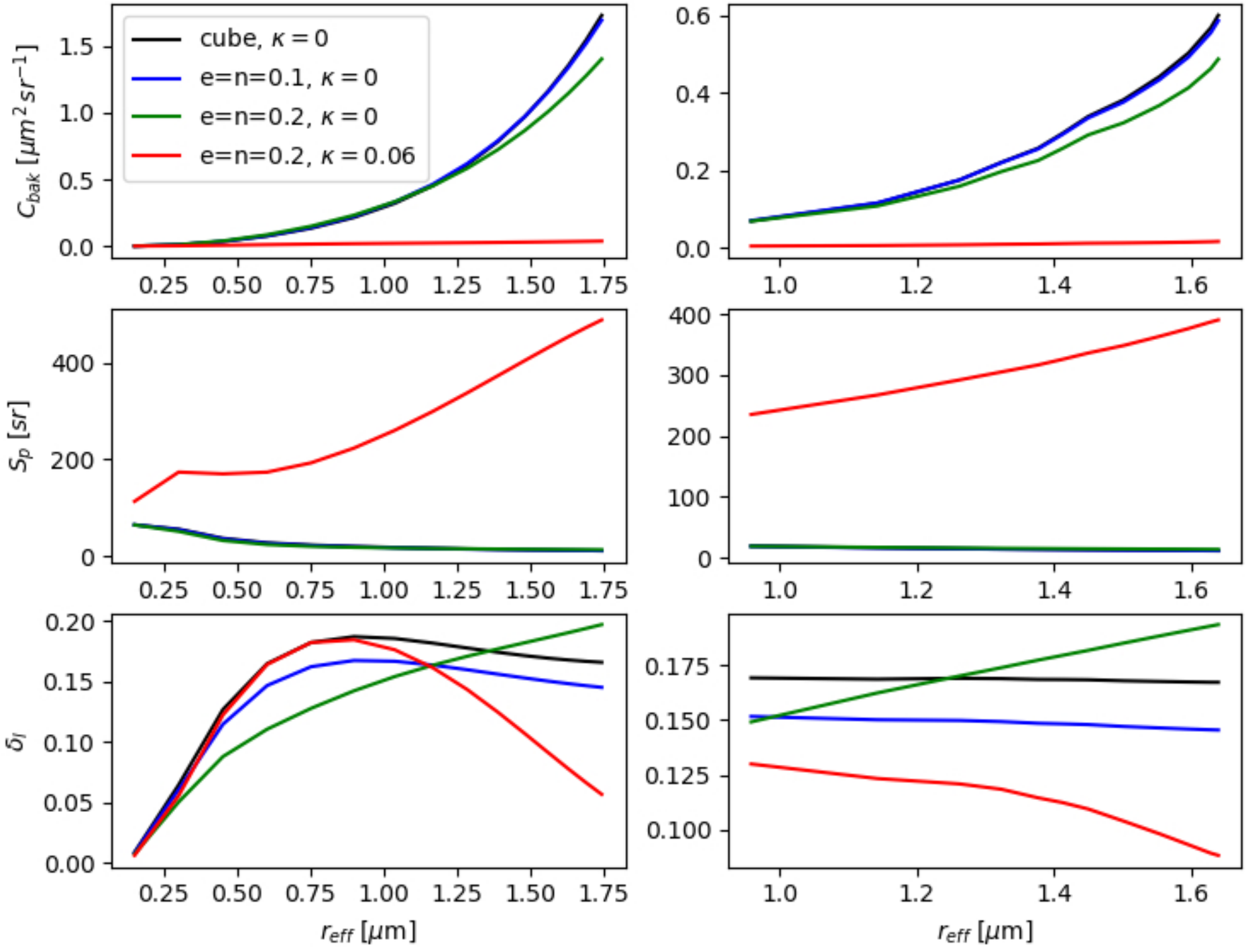
cube, $\kappa = 0$
e=n=0.1, $\kappa = 0$
e=n=0.2, $\kappa = 0$
e=n=0.2, $\kappa = 0.06$
C_{bak} [$\mu m^2 sr^{-1}$]
S_p [sr]
δ_l
r_{eff} [μm]
r_{eff} [μm]

Figure 16.

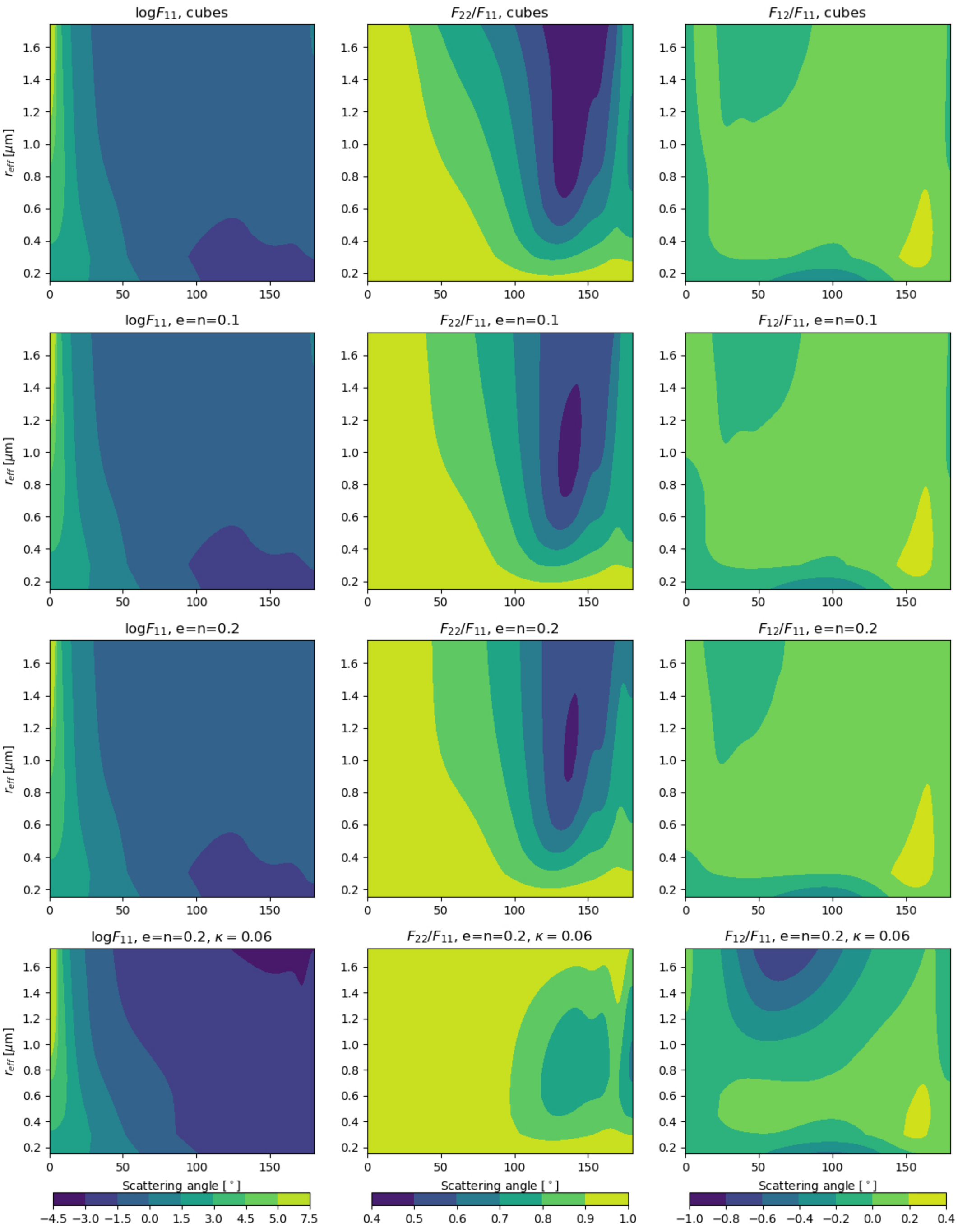
logF_{11}, cubes
F_{22}/F_{11}, cubes
F_{12}/F_{11}, cubes
logF_{11}, e=n=0.1
F_{22}/F_{11}, e=n=0.1
F_{12}/F_{11}, e=n=0.1
logF_{11}, e=n=0.2, $\kappa = 0.06$
F_{22}/F_{11}, e=n=0.2, $\kappa = 0.06$
F_{12}/F_{11}, e=n=0.2, $\kappa = 0.06$
r_{eff} [μm]
Scattering angle [°]
−4.5 −3.0 −1.5 0.0 1.5 3.0 4.5 5.0 7.5
0.4 0.5 0.6 0.7 0.8 0.9 1.0
−1.0 −0.8 −0.6 −0.4 −0.2 0.0 0.2 0.4